Article

Charge-Transfer-Induced Predissociation in Rydberg States of Molecular Cations: MgAr⁺

Dominik Wehrli, Matthieu Génévriez, Stefan Knecht, Markus Reiher, and Frédéric Merkt*
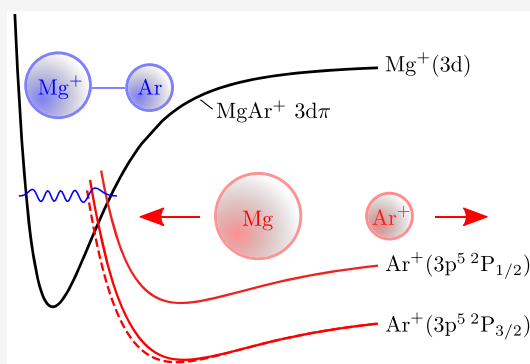
Read Online

ACCESS | Metrics & More | Article Recommendations

ABSTRACT: Very little is known about the Rydberg states of molecular cations, i.e., Rydberg states having a doubly charged ion core. With the example of MgAr⁺, we present general features of the structure and dynamics of the Rydberg states of molecular cations, which we find are subject to the process of charge-transfer-induced predissociation. Our study focuses on the spectrum of low-n Rydberg states with potential-energy functions associated with the $Mg^+(3d$ and $4s) + Ar(^1S_0)$ dissociation asymptotes. In particular, we have recorded spectra of the $3d\pi_{\Omega'}$ ($\Omega' = \frac{1}{2}, \frac{3}{2}$) Rydberg states, extending from the lowest ($v' = 0$) vibrational levels to their dissociation limits. This spectral range encompasses the region where the onset of predissociation by interaction with the mostly repulsive $^2\Sigma$ and $^2\Pi$ charge-transfer states associated with the $Mg(3s^2) + Ar^+(^2P_{1/2,3/2})$ dissociation asymptotes is observed. This interaction leads to very strong perturbations of the $3d\pi$

Rydberg states of MgAr⁺, revealed by vibrational progressions exhibiting large and rapid variations of the vibrational intervals, line widths, and spin−orbit splittings. We attribute the anomalous sign and magnitude of the spin−orbit coupling constant of the $3d\pi$ state to the interaction with a $^2\Pi$ Rydberg state correlating to the $Mg^+(4p) + Ar(^1S_0)$ dissociation limit. To analyze our spectra and elucidate the underlying process of charge-transfer-induced predissociation, we implemented a model that allowed us to derive the potential-energy functions of the charge-transfer states and to quantitatively reproduce the experimental results. This analysis characterizes the main features of the dynamics of the Rydberg series converging to the ground state of MgAr²⁺. We expect that the results and analysis reported here are qualitatively valid for a broader range of singly charged molecular cations, which are inherently prone to charge-transfer interactions.

1. INTRODUCTION

High-resolution spectroscopic data on the electronically excited states of molecular cations are scarce, particularly on their Rydberg states. At the same time, Rydberg states of molecular cations are known to play an important role as transient resonances in ion-neutral collisions[1−4] and in plasmas.[5−9] Now that photoionization studies of molecular cations are becoming feasible at synchrotron and free-electron-laser facilities, the prospects of systematic studies of Rydberg states of molecular cations are excellent.[10−12] Rydberg electrons are primarily located outside the ionic core, so that, in first approximation, Rydberg states have potential-energy functions that closely resemble those of the ion-core electronic states to which the Rydberg series converge.[13−17] In the case of molecular cations $M^+ = F_1F_2^+$, the ionic core (M^{2+}) is doubly charged and prone to dissociation into two charged atomic or molecular fragments $F_1^+ + F_2^+$ on a repulsive Coulomb potential (see Figure 1a). This situation does not favor the observation of discrete structures associated with Rydberg states (principal quantum number n) in the spectra of molecular cations, except
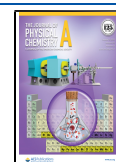
those associated with shallow potential wells at long-range resulting from charge−induced-dipole interactions between F_i^+ and $F_j(n)$ ($i, j = 1, 2$). Such long-range wells are well-known for few-electron diatomic molecules such as $H_2^{+1,18−20}$ and $HeH^{+}.^{21−23}$

The situation is qualitatively different when the doubly charged ion core $F_1F_2^{2+}$ is thermodynamically stable, or metastable with a potential well lying above the dissociation asymptote, as is the case, e.g., for $He_2^{2+}.^{24−26}$ The case of interest in the present study is illustrated in Figure 1b and arises when the ionization energy of F_1^+ is smaller than that of F_2. In this case, the ground electronic state can have a well
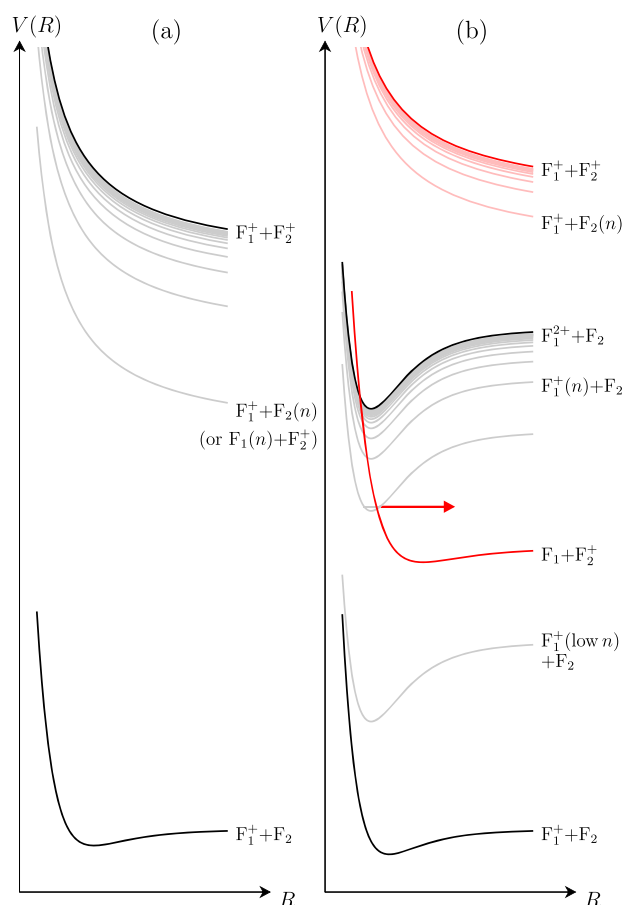
Figure 1. Potential-energy functions of the Rydberg states of molecular cations, which form series converging on the low-lying electronic states of dications $F_1F_2^{2+}$ (F_1 and F_2 designate the two fragments). (a) Molecular cation with a first ionization threshold that leads to a repulsive state, for instance H_2^+. Whereas the ground state is bound by charge–induced-dipole and perhaps valence interactions, the Rydberg states are essentially repulsive because the Rydberg electron is mostly outside the repulsive $F_1F_2^{2+}$ core. (b) Molecular cation with a first ionization limit corresponding to a thermodynamically stable dication. The repulsive charge-transfer states (red) tend to cross Rydberg states converging to the first ionization threshold, which may lead to fast predissociation (red arrow).
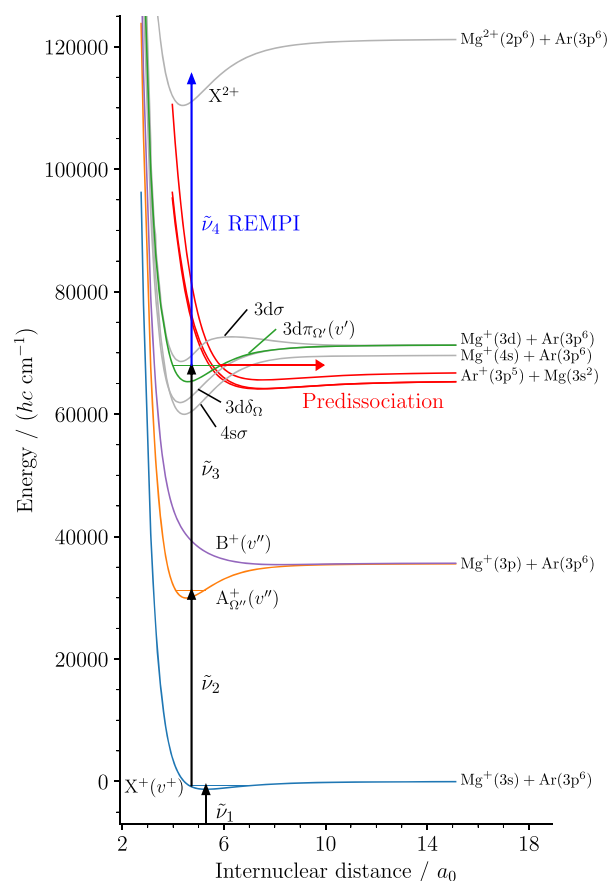

Figure 2. Excitation scheme to study the $3d\pi_{1/2}$ and $3d\pi_{3/2}$ states of MgAr$^+$. The *ab initio* potential-energy functions for the X$^+$ $^2\Sigma^+$, A$^+$ $^2\Pi_{\Omega''}$, B$^+$ $^2\Sigma^+$, $4s\sigma$, $3d\delta_\Omega$, $3d\pi_{\Omega'}$, and $3d\sigma$ states are from ref 35. The potential-energy functions of the charge-transfer states correlating to the Mg($3s^2$) + Ar$^+$(^2P_J) dissociation limits, shown by the red curves, are from this work. The potential-energy function of the X^{2+} $^1\Sigma^+$ ground state of MgAr^{2+} is from ref 28.

depth of more than 1 eV, arising from the strong charge–induced-dipole interaction between F_1^{2+} and F_2. Sharp spectral structures in the Rydberg manifold of $F_1F_2^+$ are expected, provided that rapid charge-transfer-induced predissociation into $F_1 + F_2^+$ does not render the Rydberg spectrum diffuse or prevent its observation altogether (see the red arrow in Figure 1b). One can indeed anticipate (see Section 5) that the repulsive part of the potentials associated with charge-transfer states correlating at long-range with $F_1 + F_2^+$ should cross the Rydberg-state potentials near their equilibrium positions. This was for example used to measure resonance-enhanced multiphoton dissociation spectra in CS$_2^+$.[27]

So far, only one thermodynamically stable diatomic dication, MgAr^{2+}, has been characterized spectroscopically.[28] Its ground electronic state is strongly bound $\left(D_0 = 10690(3)\,\text{cm}^{-1},^{28}\ R_e = 2.318\,\text{Å}^{29}\right)$, and one thus expects the full Rydberg manifold of MgAr$^+$ to be observable. Energetically bound Rydberg states of MgAr$^+$ are expected to cluster below the successive dissociation limits Mg$^+$(nl) + Ar($^1S_0$). The A$^+$ $3p\pi$ and B$^+$ $3p\sigma$ states of MgAr$^+$, correlating with the Mg$^+$($3p$) + Ar($^1S_0$)

dissociation limit, have been fully characterized.[30−36] Higher Rydberg states have, however, not yet been reported, except for a few long-lived vibrational levels of the $3d\pi$ state located below the Mg$^+$($3d$) + Ar($^1S_0$) dissociation limit, which were used as intermediate levels to record high-resolution photoelectron spectra of MgAr$^+$.[28]

We report here on the full characterization of the $3d\pi$ state and the observation of the $4s\sigma$ Rydberg state of MgAr$^+$. These states both lie above the Mg($3s^2$) + Ar$^+$(^2P_J) dissociation limit (see Figure 2) and are therefore ideally suited to quantify, for the first time, the effects of charge-transfer-induced predissociation on the structure and dynamics of the Rydberg states of a molecular cation by high-resolution spectroscopy.

The relevant potential-energy curves of the 3s,p,d and 4s Rydberg states of MgAr$^+$ from refs 28 and 35 are presented in Figure 2. They are crossed in their attractive region by the repulsive part of the potentials of the $^2\Sigma$ and $^2\Pi$ charge-transfer states associated with the Mg($3s^2$) + Ar$^+$(^2P_J) dissociation asymptotes and conform to the generic aspects of the Rydberg manifolds of molecular ions $F_1F_2^+$ having a thermodynamically stable doubly charged ion core $F_1F_2^{2+}$ (compare with Figure 1b). The methods we employed to record the Rydberg spectra of MgAr$^+$ and to analyze their structure are expected to be applicable to a broad range of molecular systems.
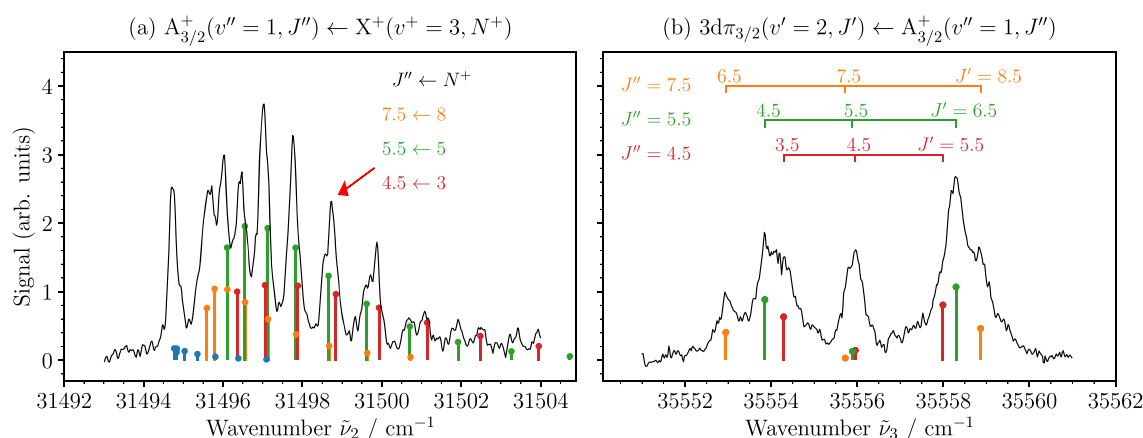
Figure 3. (a) Spectrum of the $A_{3/2}^+(v''=1) \leftarrow X^+(v^+=3)$ transition of MgAr$^+$. The blue, orange, green, and red sticks correspond to individual lines of the rotational branches with $J'' - N^+$ values of $-3/2$, $-1/2$, $+1/2$, and $+3/2$, respectively. (b) Spectrum of the $3d\pi_{3/2}(v'=2) \leftarrow A_{3/2}^+(v''=1)$ recorded after selecting the $A_{3/2}^+$ levels with $J'' = 4.5$, 5.5, and 7.5 at the position marked with a red arrow in panel a. See text for details.

In the remainder of this article, we use the following nomenclature to designate the rovibronic states of MgAr$^+$. The ground state ($^2\Sigma^+$ symmetry) is denoted as $X^+(v^+, N^+)$, where v^+ and N^+ are the vibrational and rotational quantum numbers, respectively. The first electronically excited states, which correlate to the Mg$^+$(3p ^2P_J) + Ar($^1S_0$) dissociation limits, are denoted as $A_{\Omega'}^+(v'', J'')$ ($^2\Pi_{\Omega''}$ symmetry) and $B^+(v'')$ ($^2\Sigma^+$ symmetry), with the vibrational and rotational quantum numbers v'' and J''. Higher-lying Rydberg states, which correlate to Mg$^+$(nl) + Ar($^1S_0$) dissociation limits, are denoted as $nl\lambda_{\Omega'}(v', J')$. For instance, the label $3d\pi_{3/2}(v', J')$ designates the $^2\Pi_{3/2}$ state with dissociation limit Mg$^+$(3d $^2D_{3/2}$) + Ar($^1S_0$) and vibrational and rotational quantum numbers v' and J', respectively. In cases where the rovibrational quantum numbers are not relevant for the discussion, they are omitted for legibility. If not otherwise specified, the results presented in the following are for ^{24}MgAr$^+$.

2. EXPERIMENT

The experimental setup has been described in detail in previous works.[37,38] We produced rotationally cold (~5 K) MgAr molecules in their metastable a $^3\Pi_0(v = 0)$ state by laser ablation of Mg in a supersonic expansion of Ar gas. After passing through a 3-mm-diameter skimmer, the molecular beam entered a cylindrical electrode stack, where it was perpendicularly intersected by the beams of up to four Nd:YAG-pumped dye lasers (25 Hz repetition rate, ~4 ns pulse duration) used to access and characterize the $3d\pi_{\Omega'}$ state of MgAr$^+$ in a resonant multiphoton excitation scheme. The electrode stack was used to apply pulsed electric fields in order to field ionize high Rydberg states and to extract photoions into a linear time-of-flight (TOF) mass spectrometer. All lasers were frequency doubled or tripled in β-barium-borate crystals to generate the desired radiation in the UV. Their fundamental wavenumbers were measured using a commercial wavemeter with a specified accuracy of 0.02 cm^{-1}. The lasers are referred to as Lasers 1 to 4 hereafter.

A typical excitation scheme to the $3d\pi_{\Omega'}$ state is shown as black arrows in Figure 2. Depending on the vibrational levels and the spin−orbit component of the $3d\pi_{\Omega'}$ state, different intermediate states and detection schemes had to be used. Using Laser 1, we excited MgAr from the metastable a $^3\Pi_0$ state to $[X^+(v^+)]nl$ Rydberg states, with $v^+ = 3$ or 7 and n ~

130. Laser 2, delayed by ~10 ns, then excited the MgAr$^+$ ionic core to a rovibrational level of the $A_{1/2}^+$, $A_{3/2}^+$, or B^+ state. Spectra of the transitions from the $A_{1/2}^+$, $A_{3/2}^+$, or B^+ states to the $3d\pi_{\Omega'}(v')$ levels were then recorded by tuning the frequency of Laser 3.

Transitions to the $3d\pi_{1/2}(v' \geq 5)$ and $3d\pi_{3/2}(v' \geq 3)$ core levels were detected by monitoring the charge-transfer-induced predissociation, which produced Mg atoms in their ground state and Ar atoms in a high Rydberg state (see horizontal red arrow in Figure 2). The application of a ~5-μs-long weak electric-field prepulse of −1.7 V/cm spatially separated prompt Ar$^+$ ions generated by the laser pulses from the Ar Rydberg states in the electrode stack. A subsequent strong electric-field pulse of +172 V/cm was used to field ionize the Ar Rydberg states and extract all ions toward a microchannel-plate detector located at the end of the TOF tube. The spatial separation of the Ar atoms in Rydberg states from the prompt ions allowed us to distinguish them in the TOF spectrum. In this way, the predissociation products could be detected free of background as a function of the wavenumber $\tilde{\nu}_3$ of Laser 3. The process of dissociation of the ionic core within the orbit of a Rydberg electron and the subsequent detection of a Rydberg state by pulsed-field ionization are described in detail in ref 34.

Spectra of the transitions to the $3d\pi_{1/2}(v'<5)$ and $3d\pi_{3/2}(v'<3)$ levels, which are not strongly affected by charge-transfer-induced predissociation, were measured by resonance-enhanced multiphoton ionization (REMPI) to MgAr^{2+} using Laser 4 at a fixed wavenumber of $\tilde{\nu}_4 = 46290$ cm^{-1}. In this way, we recorded the MgAr^{2+} signal as a function of the wavenumber $\tilde{\nu}_3$ of Laser 3, also under background-free conditions.

3. EXPERIMENTAL RESULTS

We have measured transitions to vibrational levels (v') of the $3d\pi_{1/2}$ and $3d\pi_{3/2}$ states of ^{24}MgAr$^+$ ranging from $v' = 0$ up to the dissociation limit. The lowest levels, i.e., $3d\pi_{1/2}(v' \leq 5)$ and $3d\pi_{3/2}(v' \leq 4)$, are sufficiently long-lived so that their rotational structure could be partially resolved. Higher-lying levels are too short-lived for any rotational structure to be observable. To unambiguously assign the vibrational quantum number v', we measured spectra of the transitions to the $3d\pi_{3/2}(v'=3-7, 9, 10)$ levels of ^{26}MgAr$^+$ and performed an isotopic-shift analysis. Just below the Mg$^+$(4s) + Ar($^1S_0$) dissociation asymptote, we

Table 1. Measured Transitions to the 3d$\pi_{\Omega'}$(v') States of ^{24}MgAr$^+$ [a]

v'	v''	Ω'	initial state	$\tilde{\nu}_{v'v''}$	$T_{v'}$	$B_{v'}$	$\Gamma_{v'}$
0	0	$^1/_2$	A$^+_{1/2}$	35352.9(3)	0.0(3)	0.192(3)	–
0	0	$^3/_2$	A$^+_{3/2}$	35313.94(20)	38.03(22)	0.1907(20)	–
1	0	$^1/_2$	A$^+_{1/2}$	35610.17(10)	257.27(14)	0.1883(17)	–
1	0	$^3/_2$	A$^+_{3/2}$	35570.58(10)	294.67(14)	0.1885(16)	–
2	1	$^1/_2$	A$^+_{1/2}$	35596.20(10)	509.28(14)	0.182(3)	–
2	1	$^3/_2$	A$^+_{3/2}$	35556.09(17)	545.54(20)	0.185(4)	–
3	1	$^1/_2$	A$^+_{1/2}$	35842.13(10)	755.21(14)	0.1813(13)	–
3	1	$^3/_2$	A$^+_{3/2}$	35801.31(10)	790.76(14)	0.1853(16)	–
4	2	$^1/_2$	A$^+_{1/2}$	35823.01(10)	995.64(14)	0.1778(22)	–
4	1	$^3/_2$	A$^+_{3/2}$	36040.49(10)	1029.94(14)	0.179(3)	–
5	2	$^1/_2$	A$^+_{1/2}$	36057.46(10)	1230.09(14)	0.1739(11)	–
5	5	$^3/_2$	A$^+_{3/2}$	35277.2(19)	1264.4(19)	–	9.4(24)
6	5	$^1/_2$	A$^+_{1/2}$	35543.90(20)	1456.60(22)	–	1.00(20)
6	5	$^3/_2$	A$^+_{3/2}$	35500(4)	1487(4)	–	18(4)
7	5	$^1/_2$	A$^+_{1/2}$	35763.7(10)	1676.4(14)	–	5.7(17)
7	8	$^1/_2$	A$^+_{1/2}$	35082(5)	1676.4(14)	–	5.7(17)
7	5	$^3/_2$	A$^+_{3/2}$	35721(7)	1708(7)	–	35(9)
8	8	$^1/_2$	A$^+_{1/2}$	35303(7)	1897(7)	–	36(9)
8	8	$^3/_2$	A$^+_{3/2}$	35290(30)	1950(30)	–	160(40)
9	8	$^1/_2$	A$^+_{1/2}$	35523(15)	2117(15)	–	77(19)
9	8	$^3/_2$	A$^+_{3/2}$	35499(10)	2166(10)	–	50(13)[b]
10	8	$^1/_2$	A$^+_{1/2}$	35738(10)	2329(4)	–	17(5)
10	12	$^1/_2$	A$^+_{1/2}$	34920(3)	2329(4)	–	17(5)
10	8	$^3/_2$	A$^+_{3/2}$	35690(3)	2357(3)	–	15(4)[b]
11	12	$^1/_2$	A$^+_{1/2}$	35111.3(24)	2520.4(24)	–	12(3)
11	12	$^3/_2$	A$^+_{3/2}$	35091(8)	2572(8)	–	38(10)
12	12	$^1/_2$	A$^+_{1/2}$	35320(4)	2729(4)	–	20(5)
12	12	$^3/_2$	A$^+_{3/2}$	35272(4)	2752(4)	–	21(5)
13	12	$^1/_2$	A$^+_{1/2}$	35499(3)	2908(3)	–	14(3)
13	12	$^3/_2$	A$^+_{3/2}$	35473(4)	2953(4)	–	22(5)[b]
14	12	$^1/_2$	A$^+_{1/2}$	35686(3)	3094.0(19)	–	9.0(23)
14	18	$^1/_2$	A$^+_{1/2}$	34668.0(15)	3094.0(19)	–	9.0(23)
14	12	$^3/_2$	A$^+_{3/2}$	35643(7)	3125(3)	–	13(4)
14	18	$^3/_2$	A$^+_{3/2}$	34630.6(22)	3125(3)	–	13(4)
15	12	$^1/_2$	A$^+_{1/2}$	35871.3(10)	3279.8(10)	–	4.9(12)
15	18	$^1/_2$	A$^+_{1/2}$	34853.6(10)	3279.8(10)	–	4.9(12)
15	12	$^3/_2$	A$^+_{3/2}$	35822.8(6)	3303.2(6)	–	3.0(7)
16	12	$^1/_2$	A$^+_{1/2}$	36038.1(9)	3447.4(11)	–	5.3(14)
16	18	$^1/_2$	A$^+_{1/2}$	35022.1(17)	3447.4(11)	–	5.3(14)
16	12	$^3/_2$	A$^+_{3/2}$	35998.4(19)	3478.3(22)	–	11(3)
16	18	$^3/_2$	A$^+_{3/2}$	34983(3)	3478.3(22)	–	11(3)
17	12	$^1/_2$	A$^+_{1/2}$	36197.0(10)	3606.2(13)	–	6.0(16)
17	18	$^1/_2$	A$^+_{1/2}$	35181(3)	3606.2(13)	–	6.0(16)
17	12	$^3/_2$	A$^+_{3/2}$	36154(5)	3639(3)	–	15(4)[b]
17	18	$^3/_2$	A$^+_{3/2}$	35145.6(24)	3639(3)	–	15(4)
18	18	$^1/_2$	A$^+_{1/2}$	35344.4(23)	3770.1(23)	–	11(3)
18	18	$^3/_2$	A$^+_{3/2}$	35299.6(23)	3794.2(23)	–	11(3)
19	18	$^1/_2$	A$^+_{1/2}$	35499.0(20)	3924.7(20)	–	10.0(20)
19	18	$^3/_2$	A$^+_{3/2}$	35456.1(8)	3950.7(8)	–	4.2(10)
20	18	$^1/_2$	A$^+_{1/2}$	35635.2(17)	4060.8(17)	–	8.5(21)
20	18	$^3/_2$	A$^+_{3/2}$	35603(3)	4098(3)	–	14(3)[b]
21	18	$^1/_2$	A$^+_{1/2}$	35786.2(12)	4211.9(12)	–	5.8(15)
21	18	$^3/_2$	A$^+_{3/2}$	35739(3)	4234(3)	–	15(4)[b]
22	4	$^1/_2$	B$^+$	34274.6(21)	4347.1(21)	–	10(3)
22	18	$^3/_2$	A$^+_{3/2}$	35869.7(14)	4365.2(14)	–	6.7(17)
22	4	$^3/_2$	B$^+$	34293.5(13)	4365.2(14)	–	6.7(17)
23	4	$^1/_2$	B$^+$	34400.0(21)	4472.5(21)	–	11(3)

Table 1. continued

v'	v''	Ω'	initial state	$\tilde{\nu}_{v'v''}$	$T_{v'}$	$B_{v'}$	$\Gamma_{v'}$
23	18	$^3/_2$	$A^+_{3/2}$	35998.7(6)	4493.8(6)	–	3.1(8)
23	4	$^3/_2$	B^+	34421.8(6)	4493.8(6)	–	3.1(8)
24	4	$^1/_2$	B^+	34521.7(12)	4594.2(13)	–	6.2(15)
24	18	$^3/_2$	$A^+_{3/2}$	36121.5(6)	4616.6(7)	–	3.4(8)
24	4	$^3/_2$	B^+	34544.6(7)	4616.6(7)	–	3.4(8)
25	4	$^1/_2$	B^+	34638.3(8)	4710.7(8)	–	4.0(10)
25	18	$^3/_2$	$A^+_{3/2}$	36236.4(13)	4731.7(14)	–	6.7(17)
25	4	$^3/_2$	B^+	34660.1(14)	4731.7(14)	–	6.7(17)
26	4	$^1/_2$	B^+	34748.7(10)	4821.2(10)	–	5.0(13)
26	4	$^3/_2$	B^+	34766.5(20)	4838.9(20)	–	10(3)
27	4	$^1/_2$	B^+	34851.2(18)	4923.7(18)	–	9.1(23)
27	4	$^3/_2$	B^+	34865.9(15)	4938.4(15)	–	7.4(19)
28	4	$^1/_2$	B^+	34947.3(16)	5019.8(16)	–	8.0(20)
28	4	$^3/_2$	B^+	34961.3(13)	5033.8(13)	–	6.4(16)
30	4	$^1/_2$	B^+	35120.0(19)	5192.4(19)	–	9.3(23)
30	4	$^3/_2$	B^+	35135.0(5)	5207.4(6)	–	2.7(7)
31	4	$^1/_2$	B^+	35199.2(7)	5271.7(7)	–	3.3(8)
31	4	$^3/_2$	B^+	35211.7(3)	5284.2(4)	–	1.7(4)
32	4	$^1/_2$	B^+	35272.8(9)	5345.3(9)	–	4.5(11)
32	4	$^3/_2$	B^+	35286.0(9)	5358.4(9)	–	4.4(11)
33	4	$^1/_2$	B^+	35343.2(11)	5415.7(11)	–	5.4(14)
33	4	$^3/_2$	B^+	35353.3(7)	5425.7(7)	–	3.3(8)
34	4	$^1/_2$	B^+	35403.5(3)	5476.0(4)	–	1.6(4)
35	4	$^1/_2$	B^+	35461.1(8)	5533.5(8)	–	4.1(10)
35	4	$^3/_2$	B^+	35471.1(13)	5543.5(13)	–	6.5(16)
36	4	$^1/_2$	B^+	35513.4(7)	5585.9(7)	–	3.5(9)
36	4	$^3/_2$	B^+	35521.4(11)	5593.9(11)	–	5.5(14)
37	4	$^1/_2$	B^+	35562.4(6)	5634.8(6)	–	3.0(7)
37	4	$^3/_2$	B^+	35568.7(10)	5641.2(10)	–	4.8(12)
38	4	$^1/_2$	B^+	35603.6(11)	5676.0(11)	–	5.6(14)
38	4	$^3/_2$	B^+	35610.7(15)	5683.1(15)	–	7.6(19)
39	4	$^1/_2$	B^+	35642.9(20)	5715.4(21)	–	10(3)
39	4	$^3/_2$	B^+	35648.6(9)	5721.1(10)	–	4.7(12)
40	4	$^1/_2$	B^+	35678.0(8)	5750.4(8)	–	4.0(10)
40	4	$^3/_2$	B^+	35682.7(7)	5755.2(7)	–	3.3(8)
41	4	$^1/_2$	B^+	35709.1(7)	5781.5(8)	–	3.7(9)
41	4	$^3/_2$	B^+	35712.8(6)	5785.2(6)	–	3.0(8)
42	4	$^1/_2$	B^+	35737.7(6)	5810.1(6)	–	3.0(8)
42	4	$^3/_2$	B^+	35740.3(6)	5812.8(6)	–	3.0(8)
43	4	$^1/_2$	B^+	35760.9(5)	5833.4(6)	–	2.6(7)
43	4	$^3/_2$	B^+	35764.0(5)	5836.4(6)	–	2.6(6)
44	4	$^1/_2$	B^+	35782.3(3)	5854.7(4)	–	1.5(4)
44	4	$^3/_2$	B^+	35784.6(3)	5857.1(4)	–	1.5(4)
45	4	$^1/_2$	B^+	35800.3(3)	5872.8(4)	–	1.7(4)
45	4	$^3/_2$	B^+	35802.3(3)	5874.8(4)	–	1.7(4)
46	4	$^1/_2$	B^+	35815.5(4)	5887.9(5)	–	2.1(5)
46	4	$^3/_2$	B^+	35817.7(4)	5890.1(4)	–	2.0(5)
47	4	$^1/_2$	B^+	35828.6(5)	5901.0(5)	–	1.5(5)
47	4	$^3/_2$	B^+	35829.5(5)	5901.9(5)	–	1.5(5)
48	4	$^1/_2$	B^+	35838.6(5)	5911.1(5)	–	1.5(5)
48	4	$^3/_2$	B^+	35839.5(5)	5911.9(5)	–	1.5(5)
49	4	$^1/_2$	B^+	35847.0(5)	5919.4(5)	–	1.4(5)
49	4	$^3/_2$	B^+	35847.8(5)	5920.3(5)	–	1.4(5)
50	4	$^1/_2$	B^+	35853.8(5)	5926.3(5)	–	1.5(5)
50	4	$^3/_2$	B^+	35854.7(5)	5927.1(5)	–	1.5(5)
51	4	$^1/_2$	B^+	35859.2(5)	5931.7(5)	–	1.5(5)
51	4	$^3/_2$	B^+	35860.1(5)	5932.5(5)	–	1.5(5)

Table 1. continued

v'	v''	Ω'	initial state	$\tilde{\nu}_{v'v''}$	$T_{v'}$	$B_{v'}$	$\Gamma_{v'}$
52	4	$1/2$	B$^+$	35863.2(5)	5935.6(5)	–	1.3(5)
52	4	$3/2$	B$^+$	35864.1(5)	5936.5(5)	–	1.3(5)

[a]The band origins and rotational constants for transitions to low-v' levels were obtained from the analysis of the resolved rotational structure (see Section 3.1). The band origins and widths for higher-lying vibrational levels were determined by fitting Lorentzian functions, unless specified otherwise. All measured quantities are in cm^{-1}, and the numbers in parentheses represent 1 standard deviation in units of the last digit. [b]Line position and line width determined using a Fano line shape function.

observed transitions that do not belong to vibrational progressions of the 3dπ states. We attribute them to transitions to high-lying vibrational levels of the 4sσ state.

3.1. Rotationally Resolved Spectra of the 3d$\pi_{\Omega'}$ State at Low v' Values. Figure 3a displays a rotationally resolved spectrum of the A$^+_{3/2}(v''=1,J'') \leftarrow$ X$^+(v^+=3,N^+)$ transition, which was recorded by monitoring the Mg$^+$ dissociation product as a function of the wavenumber $\tilde{\nu}_2$ of Laser 2 (see ref 36). This spectrum illustrates how the rotational states of the intermediate A$^+$ levels were selected. The sticks indicate the calculated positions and intensities of the rotational transitions for a rotational temperature of 4 K, determined using the standard expressions[13,39,40] for transitions between initial and final states that are well described by Hund's angular-momentum-coupling cases (b) and (a), respectively. Lines drawn in blue, orange, green, and red correspond to the possible rotational branches with $J'' - N^+ = -1.5, -0.5, +0.5$, and +1.5, respectively. The red arrow marks the position of Laser 2 used to select the intermediate $J'' = 4.5, 5.5$, and 7.5 rotational levels, when recording the spectrum of the 3d$\pi_{3/2}(v'=2,J')$ state depicted in Figure 3b. This spectrum shows the same characteristic features as all spectra we recorded for transitions to the 3d$\pi_{1/2}(v'\leq5)$ and 3d$\pi_{3/2}(v'\leq4)$ levels. It consists of three branches (P, Q, and R), corresponding to $J' - J'' = -1, 0$, and +1, respectively. The transitions are labeled along the assignment bars, the colors of which correspond to the selected levels, as indicated in Figure 3a. To model the relative intensities of the transitions, we used the standard expressions for transitions between two Hund's case (a) states,[13,39,40] and the results are depicted as sticks. Whereas the relative intensities of the P and R branches are in good agreement with the experimental results, the calculations underestimate the intensities of the Q-branch lines. We have no explanation for this observation. The lines in Figure 3b have a full width at half-maximum of about 0.5 cm^{-1}, which reflects a slight power broadening.

We determined the rotational line positions by fitting Gaussian functions to the spectra. The band origins $\tilde{\nu}_{v'v''}$ and rotational constants $B'_{v'}$ of the 3dπ states were determined from the rotational line positions in a least-squares fit based on the standard expression,[13,40]

$$\tilde{\nu}_3 = \tilde{\nu}_{v'v''} + B'_{v'}[J'(J'+1) - \Omega'^2] - B''_{v''}[J''(J''+1) - \Omega''^2] \qquad (1)$$

In eq 1, $B''_{v''}$ is the rotational constant of the A$^+_{\Omega''}$ state reported in ref 36. In the case of the 3d$\pi_{1/2}(v'=0)$ state, the resolution of the spectrum was not sufficient to determine the rotational constant from eq 1, and it was instead determined from linear extrapolation of the rotational constants of the higher vibrational levels. The band origin was subsequently deduced by matching the calculated rotational contour with

the contour observed experimentally. The band origins and rotational constants are listed in Table 1.

We derived the vibrational constants ω_e and $\omega_e x_e$, as well as the rotational constants B_e and α_e, from the observed positions of the rovibrational levels of the 3d$\pi_{1/2}(v'\leq5)$ and 3d$\pi_{3/2}(v'\leq4)$ states. Higher-lying levels of 3dπ states deviated strongly from a Morse-type behavior because of perturbations, as discussed below (see Figure 7, parts a and b), and were not included in this analysis. To determine the dissociation thresholds D_0, we exploited the thermodynamic cycles

$$\begin{aligned} D_0(3d\pi_{1/2}) = {}&D_0(A^+_{1/2}) + E(Mg^+\,3d\,^2D_{5/2})/(hc) \\ &- E(Mg^+\,3p\,^2P_{1/2})/(hc) - \tilde{\nu}_{00}(3d\pi_{1/2}) \end{aligned}$$

$$(2)$$

and

$$\begin{aligned} D_0(3d\pi_{3/2}) = {}&D_0(A^+_{3/2}) + E(Mg^+\,3d\,^2D_{3/2})/(hc) \\ &- E(Mg^+\,3p\,^2P_{3/2})/(hc) - \tilde{\nu}_{00}(3d\pi_{3/2}) \end{aligned}$$

$$(3)$$

for the two spin−orbit components of the 3dπ state. In the equations, $D_0(A^+_{1/2}) = 5476.7(10)$ cm^{-1} and $D_0(A^+_{3/2}) = 5491.5(10)$ cm^{-1} are the dissociation wavenumbers of the A$^+_{1/2}$ and A$^+_{3/2}$ states,[36] respectively, and $\tilde{\nu}_{00}(3d\pi_{1/2})$ and $\tilde{\nu}_{00}(3d\pi_{3/2})$ are the band origins listed in Table 1. The quantities denoted $E(Mg^+...)$ stand for the atomic level energies of Mg$^+$ (from ref 41) at the relevant dissociation limits. The molecular constants determined for the 3dπ states are summarized in Table 2.

Table 2. Molecular Constants Determined from the Analysis of the Spectra of the Low Vibrational Levels ($v' \leq 5$) of the 3d$\pi_{\Omega'}$ State of ^{24}MgAr$^+$ [a]

	3d$\pi_{1/2}$	3d$\pi_{3/2}$
D_0	5944.7(10)	5907.7(10)
ω_e	263.17(8)	262.48(6)
$\omega_e x_e$	2.857(15)	2.898(14)
B_e	0.1933(10)	0.1920(13)
α_e	0.0035(3)	0.0023(5)

[a]All data are in cm^{-1} and the numbers in parentheses represent one standard deviation in units of the last digit.

3.2. Diffuse Spectra of the 3d$\pi_{\Omega'}$ State at High v' Values. Most transitions to the 3d$\pi_{1/2}$ and 3d$\pi_{3/2}$ vibrationally excited levels were measured in overview scans from intermediate A$^+_{\Omega''}(v'')$ levels having large Franck−Condon overlap to the final states. In the following, we present selected spectra that illustrate the main characteristics of these transitions.

Figure 4 depicts overview spectra of transitions to the 3d$\pi_{3/2}(v' = 4-16)$ levels from the A$^+_{3/2}(v'')$ state with $v'' = 5$ (panel a), $v'' = 8$ (panel b), and $v'' = 12$ (panel c), which were
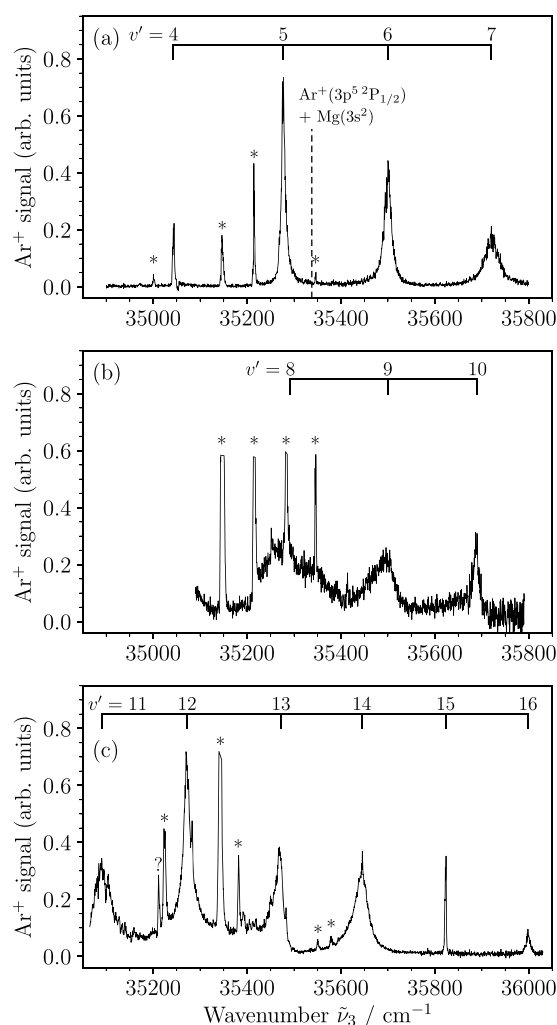
Figure 4. Overview spectra of the $3d\pi_{3/2}(v') \leftarrow A^+_{3/2}(v'')$ transitions of MgAr$^+$ with v' in the range 4−16 recorded from $A^+_{3/2}$ levels with v'' = 5 (a), v'' = 8 (b), and v'' = 12 (c). The lines marked with asterisks are spurious lines corresponding to $A^+_{\Omega''}(v'') \leftarrow X^+(v^+)$ transitions. See text for details.

recorded by monitoring the Ar$^+$ signal, as explained in Section 2. Each panel in Figure 4 covers a spectral range of 1000 cm^{-1},

such that the spectra from the different panels can be compared directly. Peaks marked with an asterisk (*) correspond to spurious $A^+_{\Omega''} \leftarrow X^+(v' = 3)$ transitions that are observable through resonant multiphoton dissociation. In the spectrum depicted in Figure 4c, we could not assign the line labeled with a question mark. The spectra show a rapid broadening and the disappearance of rotational structures of the transitions to the $3d\pi_{3/2}(v')$ levels above $v' = 4$. The observed line widths of the $3d\pi_{3/2}(v')$ levels reach a maximum at $v' = 8$ (see Figure 4b), decrease again, and then oscillate as v' increases further. The transition to $v' = 8$ is so broad that it slightly overlaps with the transition to $v' = 9$. In contrast, the transitions to $v' = 10$ and 15 are particularly narrow. The transitions to the $v' = 9$, 10, and 13 levels have asymmetric lineshapes, which can be described by Fano profiles, and the Ar$^+$ signal never returns to zero between $v' = 11$ and $v' = 13$. These observations indicate the possibility of weak direct excitation to the dissociation continuum by Laser 3. The same qualitative behavior of the line widths was also observed for the $3d\pi_{1/2}(v')$ levels (see Figure 8). The origin of the rapid variation of the line widths with v' is discussed in Section 4.

The fact that only the $3d\pi_{3/2}$ spin−orbit component is visible in Figure 4 is a consequence of the $\Delta\Omega = 0$ selection rule for transitions between initial and final states that are both well described by Hund's case (a). It results from the fact that the electron-spin projection quantum number Σ does not change in the transitions. At low vibrational excitation, the $A^+_{\Omega''}$ and the $3d\pi_{\Omega'}$ states are indeed well described by Hund's case (a), and they both have a well-defined orbital angular momentum projection quantum number of $|\Lambda| = 1$. Close to the dissociation limit, the states are better described in Hund's case (c), see ref 36, and this selection rule breaks down.

The overview spectrum of the $3d\pi_{1/2}(v') \leftarrow A^+_{1/2}(v''=18)$ transitions in the region $v' = 17-21$ is depicted in Figure 5. Next to the transitions to the $3d\pi_{1/2}(v')$ levels, additional lines, marked with asterisks, can be attributed to $A^+_{\Omega''} \leftarrow X^+(v' = 3)$ transitions. The remaining lines, which exhibit asymmetric lineshapes or are only visible as shoulders, are tentatively assigned to transitions to excited vibrational levels of the $4s\sigma$ state because the line positions match a vibrational progression that ends at the Mg$^+$(4s) + Ar($^1S_0$) dissociation limit (see also Figure 6). Vibrational levels of the $3d\delta_\Omega$ and $3d\sigma$ states can be ruled out because the associated Franck−Condon factors
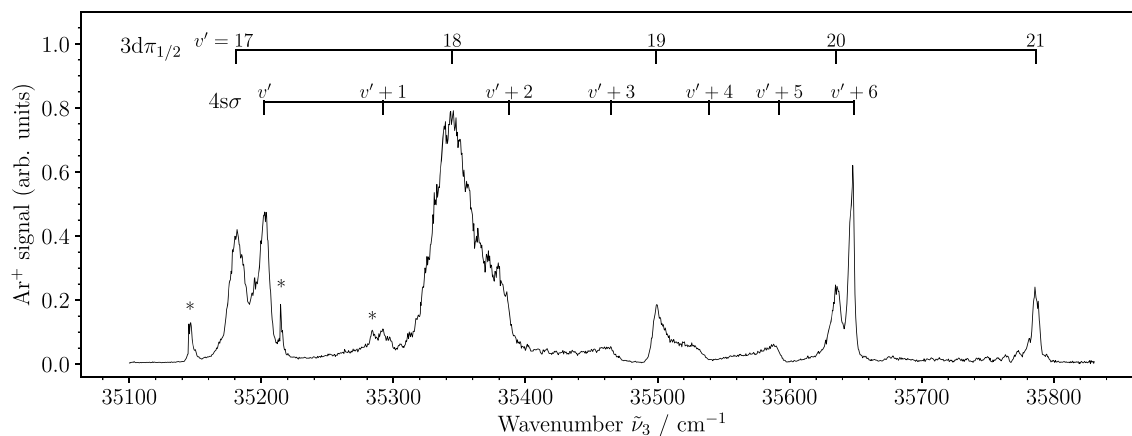

Figure 5. Overview spectrum of MgAr$^+$ recorded from the $A^+_{1/2}(v''=18)$ intermediate level and showing transitions to the $3d\pi_{1/2}(v'=17-21)$ levels, as well as transitions to vibrationally excited levels of the $4s\sigma$ state. The lines marked by asterisks are spurious lines of the $A^+_{\Omega''} \leftarrow X^+$ band system.
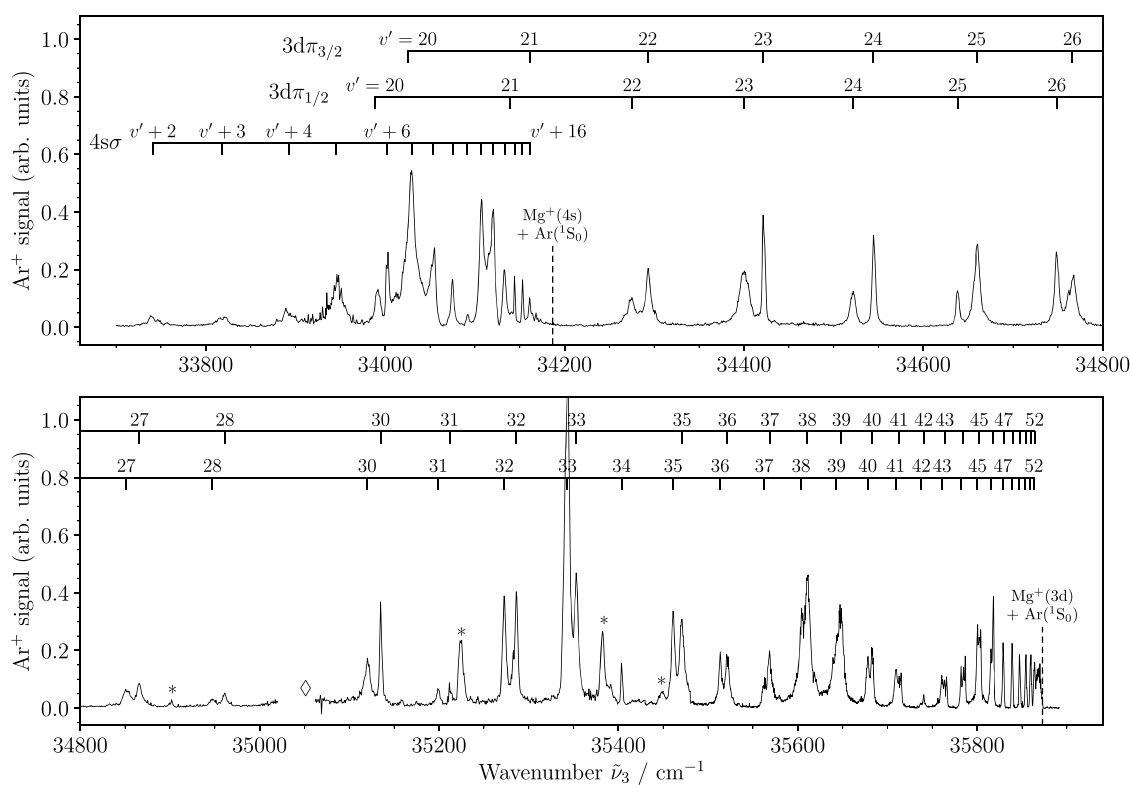
Figure 6. Overview spectrum of the $3d\pi_{\Omega'}(v') \leftarrow B^+(v''=4)$ transitions of MgAr$^+$ in the region from $v' = 18$ to the Mg$^+$(3d) + Ar(^{1}S$_0$) dissociation limit, marked by a dashed vertical line in the lower panel. In the low-wavenumber part below the Mg$^+$(4s) + Ar(^{1}S$_0$) dissociation limit designated by a dashed vertical line in the upper panel, the spectrum also reveals transitions to the highest vibrational levels of the $4s\sigma$ state. Lines marked with asterisks correspond to spurious lines of the $A^+_{\Omega''} \leftarrow X^+$ band system. The region designated by a diamond corresponds to a region dominated by the Mg 3s3p $\leftarrow$ 3s^2 transition where no reliable intensities could be measured.

calculated from the potential-energy functions in Figure 2 are too small. The results obtained for the $3d\delta_\Omega$ state will be presented in a separate publication. The small intensity fluctuations with a period of about 10 cm^{-1} which are present in some parts of the spectrum, e.g., between 35740 and 35780 cm^{-1}, are caused by fluctuations in the laser pulse energies. The transition to the $3d\pi_{1/2}(v'=18)$ level is saturated in this spectrum and was remeasured at lower laser pulse energies (not shown) for the analysis.

Figure 6 shows the overview spectrum of both $3d\pi_{\Omega'}$ spin–orbit components from $v' = 20$ up to their dissociation limits recorded via the intermediate $B^+(v'' = 4)$ state. Because the $B^+(v''=4)$ state is well described by Hund's case (b), transitions to both $3d\pi$ spin–orbit components are allowed. In the spectrum, asterisks indicate again spurious $A^+_{\Omega''} \leftarrow X^+(v' = 3)$ transitions. The region around 35051 cm^{-1} designated by a diamond ($\Diamond$) corresponds to the atomic Mg 3s3p $\leftarrow$ 3s^2 transition. In this region, the Mg$^+$ ion signal was so strong that it saturated the detection system and prevented the measurement of reliable intensities. Above $v' = 22$, the spin–orbit splitting of the $3d\pi_{\Omega'}$ state decreases and can no longer be resolved above $v' = 47$. In the range between $v' = 23$ and 30, the line widths of the $3d\pi_{1/2}$ vibrational states first decrease and then increase again, whereas the $3d\pi_{3/2}$ state exhibits the opposite behavior. The transition intensities to the $3d\pi$ states are also subject to large variations. For instance, the strong intensities for both spin–orbit components at $v' = 33$ are followed by very weak ($3d\pi_{1/2}$) or even vanishing ($3d\pi_{3/2}$) intensities at $v' = 34$. These observations indicate strong perturbations, which are analyzed in detail in Section 4.

An additional vibrational progression is observed directly below the Mg$^+$(4s) + Ar(^{1}S$_0$) dissociation limit at 34186.7 cm^{-1}. We attribute it to transitions to high vibrational levels of the $4s\sigma$ state, for the reasons presented in the discussion of Figure 5.

To determine the line positions and widths (full width at half-maximum) of the measured $3d\pi$ vibrational levels, we fitted Lorentzian functions to the corresponding lines. For a few transitions to vibrational levels of the $3d\pi_{3/2}$ state with asymmetric line shapes, we also fitted Fano profiles. The vibrational term values $T_{v'}$ and line widths $\Gamma_{v'}$ of all observed levels are listed in Table 1. The specified uncertainties in the line positions and widths correspond to 20% and 25% of the determined values for the widths, respectively. These uncertainties also take into account the fact that the vibrational bands have an underlying unresolved rotational structure. For vibrational levels that were measured from more than one initial state, the term values and widths correspond to a weighted average of all measurements. Because the spin–orbit splittings could not be resolved for $v' \geq 47$, the positions of the two $3d\pi$ spin–orbit components were estimated using the atomic spin–orbit splitting of -0.87 cm^{-1} of the Mg$^+$(3d) states,[41] which we expect to be a good approximation for the molecular spin–orbit splittings just below the dissociation limit.

The vibrational assignments presented above are based on a standard isotopic-shift analysis.[14] For the $3d\pi_{3/2}$ state we measured the positions of the vibrational levels $v' = 3-7$, 9, and 10 of ^{26}MgAr$^+$ (not shown), in addition to those of ^{24}MgAr$^+$. The isotopic shifts range from 20(5) cm^{-1} for $v' = 3$

to 49(5) cm^{-1} for $v' = 10$, which is only compatible with the vibrational assignments presented in Table 1. The corresponding vibrational constants for ^{24}MgAr$^+$ are listed in Table 2.

All level positions, level widths, and molecular constants determined in this analysis of the 3d$\pi_{\Omega'}$ state of MgAr$^+$ are presented in Tables 1 and 2. The data obtained for both spin−orbit components ($\Omega' = {}^1/_2, {}^3/_2$) extend from the lowest ($v' = 0$) level all the way to the dissociation threshold beyond $v' = 50$.

To facilitate the discussion and interpretation of these observations, overviews of the observed vibrational intervals $\Delta G(v') = T_{v'+1} - T_{v'}$ are presented in panels (a) and (b) of Figure 7. The evolution of the spin−orbit splittings and the line widths with v' are presented graphically in Figure 7c and Figure 8, respectively. These data reveal pronounced perturbations above $v' = 6$, discussed in detail in the next section. Moreover, the spin−orbit splitting of the 3d$\pi_{\Omega'}$ states reaches ~40 cm^{-1} for the low-lying vibrational levels and the

states with $\Omega' = {}^1/_2$ are systematically lower in energy than those with $\Omega' = {}^3/_2$. Asymptotically, the 3d$\pi_{1/2}$ state correlates to the Mg$^+$(3d ^{2}D$_{5/2}$) + Ar(^{1}S$_0$) dissociation limit whereas the 3d$\pi_{3/2}$ state correlates to the Mg$^+$(3d ^{2}D$_{3/2}$) + Ar(^{1}S$_0$) limit. In the Mg$^+$ ion, the spin−orbit splitting of the 3d ^{2}D$_{3/2}$ and ^{2}D$_{5/2}$ states is -0.87 cm^{-1}.[41] Using the model of Cohen and Schneider,[42] we would expect a spin−orbit splitting of the 3d$\pi_{\Omega'}$ states on the order of ${}^2/_5 \times (-0.87) = -0.35$ cm^{-1}, the $\Omega' = {}^3/_2$ levels being lower in energy than the $\Omega' = {}^1/_2$ ones. Our experimental results show instead a splitting that is inverted and up to 2 orders of magnitude larger. The origin of this behavior is discussed in detail in Section 4.3.

4. ANALYSIS AND DISCUSSION

4.1. Theoretical Model. To explain the experimental results and the strong perturbations for both spin−orbit components of the 3dπ state, in particular those affecting the line widths and level energies, we employed a model that describes the interaction of the 3dπ states with the energetically close-lying and essentially repulsive charge-transfer (CT) states associated with the Mg(3s^2) + Ar$^+$(3p^5 ^{2}P$_{1/2}$) and Mg(3s^2) + Ar$^+$(3p^5 ^{2}P$_{3/2}$) dissociation limits. For the description of the two spin−orbit components of the 3dπ states we used the *ab initio* potential-energy functions published in ref 35. The relevant molecular constants obtained from these potential-energy functions are $D_0 = 5873$ cm^{-1}, $\omega_e = 263.5$ cm^{-1}, and $\omega_e x_e = 2.82$ cm^{-1} and $D_0 = 5836$ cm^{-1}, $\omega_e = 262.9$ cm^{-1}, and $\omega_e x_e = 2.83$ cm^{-1} for the 3d$\pi_{1/2}$ and 3d$\pi_{3/2}$ states, respectively. These theoretical values are in good agreement with those determined experimentally (see Table 2). No accurate *ab initio* calculations are available for the CT states. Consequently, we used the indirect information on these states that are encoded in the perturbations of the 3dπ states to construct their potential-energy functions based on model potentials.

In first approximation, the potential-energy functions of the CT states correspond to the eigenvalues of the matrix[13,42,43]

$$\begin{pmatrix} V_\Sigma(R) & \dfrac{a}{\sqrt{2}} & 0 \\[2ex] \dfrac{a}{\sqrt{2}} & V_\Pi(R) - \dfrac{a}{2} & 0 \\[2ex] 0 & 0 & V_\Pi(R) + \dfrac{a}{2} \end{pmatrix}$$

$$\quad (4)$$

where $V_\Sigma(R)$ and $V_\Pi(R)$ are the diabatic potential-energy curves of the CT states of Σ and Π symmetry (R is the internuclear distance), and $a = -954.389$ cm^{-1} is the spin−orbit coupling constant, which is assumed to be independent of R and corresponds to the atomic spin−orbit splitting $3a/2$ between the Ar$^+$(^{2}P$_{1/2}$) and Ar$^+$(^{2}P$_{3/2}$) states. We denote the eigenvalues of eq 4 as $V_{1/2}^+$, $V_{1/2}^-$, and $V_{3/2}$, where the subscript represents the total-angular-momentum projection quantum number Ω and the superscripts + and − denote the larger and smaller of the two eigenvalues with $\Omega = {}^1/_2$. The diabatic potential-energy functions are modeled with the functions

$$V_\Lambda(R) = A_\Lambda e^{-b_\Lambda R} - \frac{\alpha_{Mg}}{2R^4} f_4(R) \quad (5)$$

which consist of a repulsive Born−Mayer term[44] and a charge−induced-dipole attractive long-range term. In eq 5, A_Λ and b_Λ are adjustable parameters that depend on the angular-
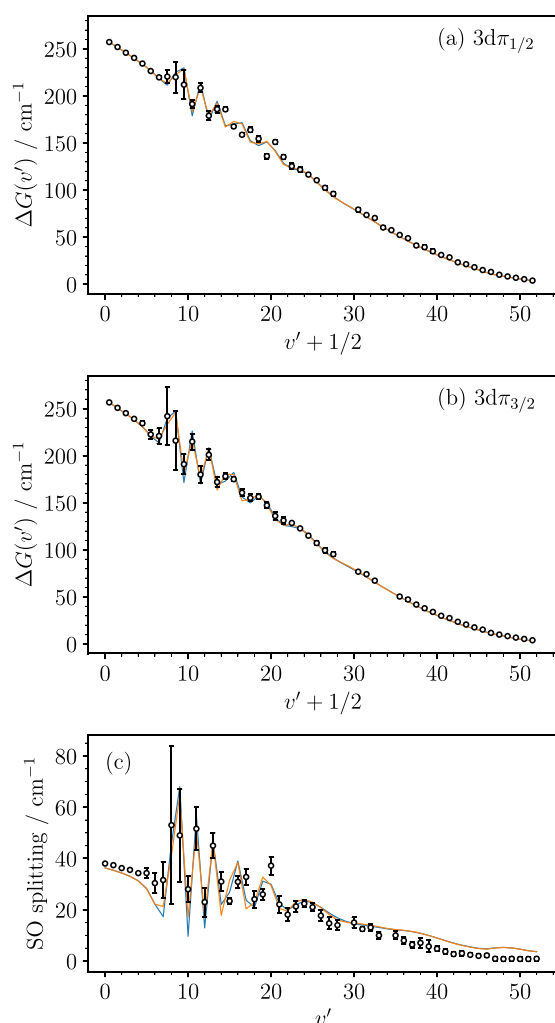

Figure 7. Vibrational intervals $\Delta G(v') = T_{v'+1} - T_{v'}$ of the 3d$\pi_{1/2}$ (a) and 3d$\pi_{3/2}$ (b) states and spin−orbit splittings of the 3d$\pi_{\Omega'}$ state of MgAr$^+$ (c). The open circles with error bars correspond to experimental data, the orange lines to exterior-complex-scaling calculations of the predissociation interactions between the 3dπ states and the repulsive states correlating to the Mg(3s^2) + Ar$^+$(^{2}P$_J$) dissociation limits, and the blue lines to approximate perturbative calculations based on the same method.
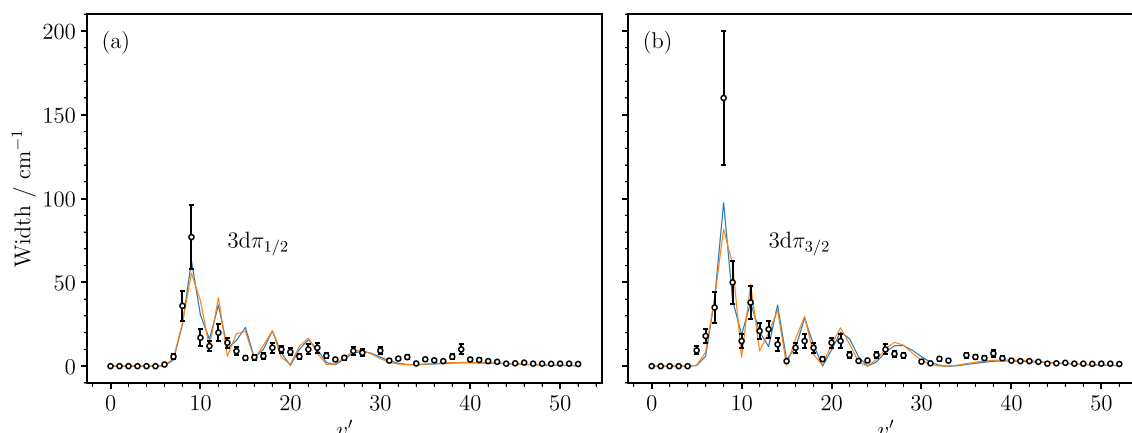
Figure 8. Predissociation widths of the vibrational levels of the $3d\pi_{\Omega'}$ states with $\Omega' = {}^1\!/_2$ (a) and $\Omega' = {}^3\!/_2$ (b). The open circles with vertical error bars correspond to the experimental data. The full lines represent the results of exterior-complex-scaling calculations using the same color code as in Figure 7 (see text for details).

momentum projection quantum number Λ ($\Lambda = 0, 1$), $\alpha_{Mg} = 71.2\ a_0^3$ is the polarizability volume of ground-state Mg,[45] and

$$f_4(R) = 1 - e^{-b_\Lambda R} \sum_{k=0}^{4} \frac{(b_\Lambda R)^k}{k!} \qquad (6)$$

is the Tang–Toennies damping function.[46] The values of A_Λ and b_Λ are given in Table 3, and their determination is discussed below. The potential functions for the CT states depicted in Figure 2 correspond to these values.

Table 3. Model Parameters (A_Λ, b_Λ) Determined to Describe the Potential-Energy Functions of the Charge-Transfer States Correlating to the $Mg(3s^2) + Ar^+({}^2P_J)$ Dissociation Limit and the Interactions (H_{int}) between These States and the $3d\pi$ States According to Equations 8 and 9

A_Σ	25 E_h
b_Σ	1.14 a_0^{-1}
A_Π	15 E_h
b_Π	1.09 a_0^{-1}
$H_{int,1/2}^+$	75 cm^{-1}
$H_{int,1/2}^-$	200 cm^{-1}
$H_{int,3/2}$	250 cm^{-1}

To determine the effect of the interaction of the $3d\pi$ states with the CT states, we first solved the nuclear Schrödinger equation,

$$\left[-\frac{1}{2\mu} \frac{d^2}{dR^2} + V(R) \right] \psi_v(R) = E_v \psi_v(R) \qquad (7)$$

separately for each potential-energy function using a Legendre–Gauss–Lobatto finite-element discrete-variable-representation (FEM-DVR) technique in combination with exterior complex scaling.[47−49] The use of exterior complex scaling permits an accurate description of the continua above the dissociation thresholds, which can be treated on the same footing as the bound states. Using the eigenstates determined from eq 7, we constructed an effective Hamiltonian matrix describing the $3d\pi$ and CT bound and continuum states, and their mutual interactions. We assume that the configuration

interaction between the $3d\pi$ and CT states preserves the projection of the total angular momentum onto the internuclear axis, thus only states with the same Ω value interact and the $\Omega = {}^3\!/_2$ and $\Omega = {}^1\!/_2$ states can be treated separately.

The matrix elements of the effective Hamiltonian matrix for $\Omega = {}^3\!/_2$ are given by

$$\langle v, 3d\pi_{3/2}|H|v', 3d\pi_{3/2}\rangle = E_{v,3d\pi_{3/2}} \delta_{vv'},$$

$$\langle v, V_{3/2}|H|v', V_{3/2}\rangle = E_{v,V_{3/2}} \delta_{vv'},$$

$$\langle v, 3d\pi_{3/2}|H|v', V_{3/2}\rangle = \int dR\ (\psi_{v,3d\pi_{3/2}}(R))^* H_{int,3/2} \psi_{v',V_{3/2}}(R) \qquad (8)$$

where $H_{int,3/2}$ describes the CT interaction between the $3d\pi_{3/2}$ state and the CT state with $\Omega = {}^3\!/_2$. The basis states in eq 8 include bound and continuum states. The eigenvalues of the effective Hamiltonian matrix associated with predissociating resonances of predominant $3d\pi_{3/2}$ character were selected by inspecting the eigenvectors. As usual in complex scaling, they possess a real part which is equal to the energy of the eigenstate and an imaginary part which is equal to $-\Gamma_v/2$, where Γ_v is the width of the eigenstate.

The interaction of the $3d\pi_{1/2}$ state with the two $\Omega = 1/2$ CT states is described by the effective Hamiltonian with matrix elements given by

$$\langle v, 3d\pi_{1/2}|H|v', 3d\pi_{1/2}\rangle = E_{v,3d\pi_{1/2}} \delta_{vv'},$$

$$\langle v, V_{1/2}^+|H|v', V_{1/2}^+\rangle = E_{v,V_{1/2}^+} \delta_{vv'},$$

$$\langle v, V_{1/2}^-|H|v', V_{1/2}^-\rangle = E_{v,V_{1/2}^-} \delta_{vv'},$$

$$\langle v, 3d\pi_{1/2}|H|v', V_{1/2}^+\rangle = \int dR\ (\psi_{v,3d\pi_{1/2}}(R))^* H_{int,1/2}^+ \psi_{v',V_{1/2}^+}(R),$$

$$\langle v, 3d\pi_{1/2}|H|v', V_{1/2}^-\rangle = \int dR\ (\psi_{v,3d\pi_{1/2}}(R))^* H_{int,1/2}^- \psi_{v',V_{1/2}^-}(R),$$

$$\langle v, V_{1/2}^+|H|v', V_{1/2}^-\rangle = 0 \qquad (9)$$

where the coupling elements $H^+_{int,1/2}$ and $H^-_{int,1/2}$ are different. In principle, these coupling elements are R-dependent. However, in the absence of reliable data, we assumed R-independent couplings, which yields results in good agreement with the experimental data while restricting the number of adjustable parameters to a minimum (see also the discussion in the next section).

4.2. Line Positions and Line Widths. Panels a and b of Figure 7 show Birge−Sponer plots[14,50] of the vibrational levels of the $3d\pi_{1/2}$ and $3d\pi_{3/2}$ states, respectively, i.e., the differences in the term values of adjacent levels, $\Delta G(v') = T_{v'+1} - T_{v'}$, versus $v' + \tfrac{1}{2}$. For the lowest vibrational levels ($v' \lesssim 5$), the data points form a straight line, indicating unperturbed states. Beyond $v' = 5$ rapid oscillations of $\Delta G(v')$ occur, which indicate perturbations. For the highest vibrational levels ($v' \gtrsim 35$), the $\Delta G(v')$ values evolve smoothly again, as do the spin−orbit splittings depicted in Figure 7c, which indicates that the perturbations become smaller in this range.

Figure 8 depicts the experimentally determined line widths of all measured states. At low v', the rotational structure could be resolved and the observed widths are limited by the instrumental resolution ($\sim$0.1 cm^{-1}). They are therefore set to zero in Figure 8. A rapid increase of the line widths is observed between $v' \sim 5$ and $v' \sim 10$, which is followed by an oscillating decrease toward the dissociation limit, as already stated in Section 3.2. The evolution of the widths with v' closely reflects the perturbations in the level positions depicted in Figure 7, which suggests that both the widths and the perturbations in the energy-level structure have the same origin.

By carefully optimizing the parameters A_Λ and b_Λ of the model potentials as well as the interaction strengths H_{int} introduced in Section 4.1, we were able to satisfactorily reproduce the experimental results with our theoretical model, the results of which are shown as full orange lines in Figures 7 and 8. All model parameters are listed in Table 3. The good agreement between the experimental results and those obtained with the theoretical model leads to the conclusion that the observed line widths and the perturbations of the vibrational level energies of the $3d\pi$ states originate from the interaction with the CT states and their associated continua. Moreover, the Ar$^+$ dissociation products detected experimentally at v' values higher than 5 are direct evidence of CT-induced predissociation, and the line widths reflect the predissociation lifetimes of the $3d\pi$ vibrational resonances.

Figure 9 shows the potential functions of the $3d\pi$ and CT states. Because the spin−orbit splitting of the $3d\pi$ states is small on the scale of the figure, the two components lie almost on top of each other. In addition, the figure depicts all measured vibrational levels of the $3d\pi_{3/2}$ state (the $3d\pi_{1/2}$ levels are not shown for clarity). The $V_{1/2}$ and $V_{3/2}$ potential curves cross the $3d\pi_{1/2}$ and $3d\pi_{3/2}$ potential curves just below their $v' = 9$ and $v' = 8$ vibrational levels, respectively, where the observed predissociation widths are largest. This observation is an illustration of the well-known fact that predissociation is fastest in the vicinity of curve crossings.[13] In principle, predissociation is possible for all v' levels, because they all lie above the Mg(3s^2) + Ar$^+$(^{2}P$_{3/2}$) dissociation limit. However, for the lowest $3d\pi$ vibrational levels ($v' \lesssim 5$) predissociation is strongly inhibited because of the vanishing Franck−Condon overlap with the CT continuum states, which explains why, in this energy region, we did not detect Ar$^+$ fragments on the time scale of our experiment.
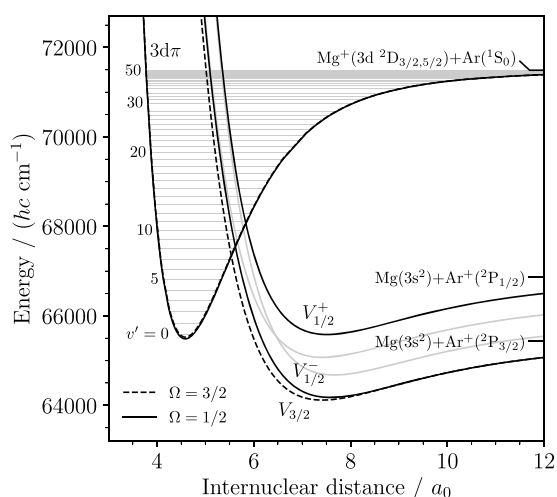

Figure 9. Potential-energy functions used to calculate the positions and predissociation widths of the vibrational levels of the $3d\pi_{\Omega'}$ state of MgAr$^+$. The full and dashed lines correlating to the Mg$^+$(3d) + Ar(^{1}S$_0$) dissociation limits correspond to the $3d\pi_{1/2}$ and $3d\pi_{3/2}$ states, respectively. The two full lines and the dashed line correlating to the Mg(3s^2) + Ar$^+$(^{2}P$_J$) dissociation limits correspond to adiabatic potential-energy functions of the two $\Omega = \tfrac{1}{2}$ states and the $\Omega = \tfrac{3}{2}$ state. The gray potential-energy curves correspond to the first two diagonal elements of the matrix in eq 4. The horizontal lines correspond to the positions of the measured vibrational levels of the $3d\pi_{1/2}$ state.

In general, the interaction strengths H_{int} depend on the internuclear distance R. However, our results show that in the present case the choice of constant H_{int} values is sufficient for a semiquantitative description of the perturbations because the coupling is only effective at R values near the crossings. The difference between the two interactions that describe the coupling to the $\Omega = \tfrac{1}{2}$ CT states ($H^+_{int,1/2} = 75$ cm^{-1} and $H^-_{int,1/2} = 200$ cm^{-1}) can be justified in terms of the Σ and Π characters of the $V^+_{1/2}(R)$ and $V^-_{1/2}(R)$ potentials of the CT states, which strongly depend on the internuclear separation. At large internuclear separations, i.e., for $R \gtrsim 8\ a_0$, the spin−orbit interaction mixes the two diabatic Hund's case (a) $\Sigma_{1/2}$ and $\Pi_{1/2}$ states with $\Omega = \tfrac{1}{2}$ (see eq 4 and the subsequent discussion) and the resulting $V^+_{1/2}(R)$ adiabatic states correspond to Hund's case (c) states. The $V^+_{1/2}(R)$ adiabatic state has a predominant Π character ($|c^+_\Pi|^2 = 0.67$), whereas the $V^-_{1/2}(R)$ state has predominant Σ character ($|c^-_\Sigma|^2 = 0.67$) in this range. As R decreases and approaches 6.4 a_0, the diagonal elements in eq 4 corresponding to $\Sigma_{1/2}$ and $\Pi_{1/2}$ become degenerate (see gray curves in Figure 9) and both $\Omega = \tfrac{1}{2}$ components become equal mixtures of Σ and Π character ($|c^\pm_\Sigma|^2 = |c^\pm_\Pi|^2 = 0.5$). Below $R \approx 6\ a_0$, the two $\Omega = \tfrac{1}{2}$ components can be well described by an almost pure Σ^+ state in the case of the $V^+_{1/2}$ potential function and an almost pure $\Pi_{1/2}$ state in the case of the $V^-_{1/2}$ potential function. In the region of the curve crossings with the $3d\pi_{1/2}$ state ($R \approx 5 - 6\ a_0$), Λ is therefore a good quantum number for all states involved. Because homogeneous ($\Delta\Lambda = 0$) perturbations are stronger than heterogeneous ($|\Delta\Lambda| = 1$) perturbations, the CT state with the $V^-_{1/2}$ potential function is coupled much more strongly to the $3d\pi_{1/2}$ state than the state with $V^+_{1/2}$ potential, which explains why $H^-_{int,1/2}$ (200 cm^{-1}) is larger than $H^+_{int,1/2}$ (75 cm^{-1}).

To gain a better understanding of the processes described in the previous paragraphs, we also calculated the level energies

and widths of the $3d\pi$ states in a perturbative treatment, in addition to the diagonalization of the complete Hamiltonians presented Section 4.1. Following Fano's procedure,[13,51] the predissociation widths that arise from the interaction of the $3d\pi_{3/2}(v')$ state (with unperturbed energy $E_{v'}$) with the continuum of the $V_{3/2}$ state are given by

$$\Gamma_{v'} = 2\pi \left| \langle \varepsilon, V_{3/2} | H_{\text{int},3/2} | v', 3d\pi_{3/2} \rangle \right|^2 \Big|_{\varepsilon = E_{v'}}$$
$$= 2\pi H_{\text{int},3/2}^2 \left| \langle E_{v'}, V_{3/2} | v', 3d\pi_{3/2} \rangle \right|^2 \quad (10)$$

where $|\varepsilon, V_{3/2}\rangle$ is an energy-normalized continuum function with energy ε. The continuum-induced energy shifts are calculated as

$$\Delta E_{v'} = \mathcal{P} \int d\varepsilon \, \frac{\left| \langle \varepsilon, V_{3/2} | H_{\text{int},3/2} | v', 3d\pi_{3/2} \rangle \right|^2}{E_{v'} - \varepsilon}$$
$$= H_{\text{int},3/2}^2 \mathcal{P} \int d\varepsilon \, \frac{\left| \langle \varepsilon, V_{3/2} | v', 3d\pi_{3/2} \rangle \right|^2}{E_{v'} - \varepsilon} \quad (11)$$

where $\mathcal{P}$ denotes the Cauchy principal value. Equations 10 and 11 are readily evaluated in the framework of exterior complex scaling, as explained in Appendix A. The widths and energy shifts of the $3d\pi_{1/2}$ levels are given by incoherent sums of the interactions with the two $\Omega = {}^1/_2$ CT states,

$$\Gamma_{v'} = \Gamma_{v'}^+ + \Gamma_{v'}^- \quad (12)$$

$$\Delta E_{v'} = \Delta E_{v'}^+ + \Delta E_{v'}^- \quad (13)$$

where the summands are calculated in the same way as in eqs 10 and 11.

The results of the perturbative calculations are depicted as blue lines in Figures 7 and 8. The agreement with the results obtained from the full calculation is so good that the blue lines are hardly distinguishable from the orange lines. This good agreement allows an interpretation of the processes based on eqs 10 and 11. In these equations, the expression of the type $|\langle \varepsilon | v' \rangle|^2$ is a Franck–Condon density, implying that the evolution of the widths and the energies with v' is almost purely governed by the overlap of the $3d\pi$ bound-state and CT continuum wave functions. This finding is also in accord with the observation that the predissociation widths are largest where the potential curves cross (see discussion above).

4.3. On the Energetic Order of the Spin–Orbit Components of the $3d\pi$ States. As discussed at the end of Section 3, there are irregularities concerning the ordering of the spin–orbit components of the $3d\pi_{\Omega'}$ state and the magnitude of the spin–orbit splitting. To resolve this issue, we complement our previous *ab initio* calculations[35] in the present work with relativistic Kramers-restricted *ab initio* complete-active-space configuration interaction (KR-CASCI) calculations[52,53] with *variationally* treated spin–orbit coupling at various Mg–Ar internuclear distances.

All KR-CASCI calculations were performed within the exact two-component Hamiltonian framework[54−56] including two-electron Coulomb and Gaunt contributions[57,58] in combination with very large, fully uncontracted aug-cc-pV5Z basis sets[59] (denoted as 5Z*) for Mg and Ar. The reference wave function at each Mg–Ar internuclear distance was obtained from an average-of-configurations self-consistent-field calculation[60] for the open-shell MgAr$^+$ ion by considering all possible configurations of seven electrons in 32 Kramers-paired

spinors (i.e., representing the Ar $3p$ and Mg $3s3p3d4s4p$ shells). The subsequent KR-CASCI correlation step encompassed the same correlation space, i.e., correlating the seven valence electrons of the MgAr$^+$ molecular ion in 32 Kramers-paired spinors denoted as KR-CASCI(7,32)/5Z*. Consequently, the KR-CASCI(7,32)/5Z* calculations reported in this work provide useful *qualitative* insight, whereas for *quantitative ab initio* data we refer the reader to our previous work.[35]

All KR-CASCI(7,32)/5Z* were carried out with the DIRAC19 program package.[61,62] Molecular constants have been derived by a least-squares fit of the potential energy curves to a fifth-order polynomial by means of the TWOFIT utility program available in DIRAC19.

Considering the qualitative nature of the KR-CASCI(7,32)/5Z* calculations, the resulting excited-state equilibrium internuclear distance of $R_e(3d\pi_{\Omega'}) = 4.67 \, a_0$ for both spin–orbit-split $3d\pi_{\Omega'}$ states is in fair agreement with the experimentally determined value of $R_e(3d\pi_{\Omega'}) \approx 4.56 \, a_0$. Moreover, we find a spin–orbit splitting of the $\Omega' = {}^1/_2, {}^3/_2$ components of approximately $33.20 \, \text{cm}^{-1}$ ($v' = 0$) which compares well with the measured value of $38.03 \, \text{cm}^{-1}$ ($v' = 0$, see Table 1). In line with the experimental data and our previous *ab initio* results,[35] the $\Omega' = {}^1/_2$ spin–orbit component of the $3d\pi_{\Omega'}$ manifold is the lower state.

Figure 10 shows the square of the CI coefficients (denoted as weight) of the leading configurations of the $3d\pi_{\Omega'}$ states as a
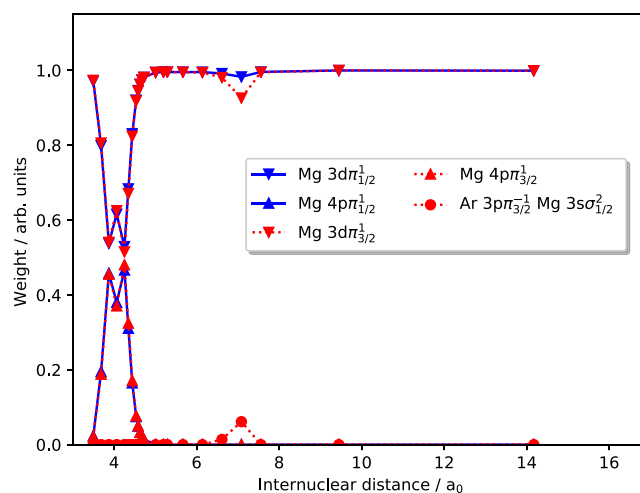

Figure 10. Squares of the CI coefficient (denoted as weight) of the leading configurations of the $3d\pi_{\Omega'}$ states as a function of the internuclear Mg−Ar distance as obtained from KR-CASCI(7,32)/5Z* calculations. Each leading configuration can be written as $[\text{Ar } 3p^6]x^1$ in a compact notation, where x denotes the nature of the additional occupied spinor(s). Blue-colored symbols refer to configurations contributing to the $3d\pi_{1/2}$ and red-colored ones to the $3d\pi_{3/2}$ state.

function of the internuclear Mg−Ar distance. The total weight for each electronic state is normalized to 1.0. As can be understood in view of Figure 10, starting from the asymptotic limit at large internuclear distances, the dominating configurations of the eigenvectors of the $3d\pi_{\Omega'}$ states (with weights of ~1.0) originate from the single occupation of a Mg $3d\pi_{\Omega'}$ spinor in addition to the closed-shell $[\text{Ar } 3p^6]$ core. When approaching the equilibrium internuclear distance toward the strongly repulsive region of the potential energy curves for the $3d\pi_{\Omega'}$ states (Mg−Ar internuclear distances smaller than ~5.0

a_0), the composition of the corresponding eigenvector markedly changes for each of the $\Omega' = {}^1/_2, {}^3/_2$ spin−orbit components as is evident from Figure 10. The additional configuration gaining simultaneously particular weight in both eigenvectors arises from the occupation of a spinor that exhibits predominantly a Mg-centered 4p character according to a Mulliken population analysis of the reference molecular spinor basis. Although such a contribution is dipole-forbidden in the asymptotic limit where the Mg^+ ion is isolated, the presence of the Ar "atom" in the $MgAr^+$ ion lifts this restriction at short internuclear distances. Moreover, since the energetic order of the spin−orbit components of the Mg 4p manifold is $p\pi_{1/2} < p\pi_{3/2}$,[41] we attribute the observed large and reversed spin−orbit splitting of the $3d\pi_{\Omega'}$ states to this somewhat unexpected configurational mixing that is most pronounced at Mg−Ar internuclear distances between 3.6 a_0 and 4.7 a_0.

Finally, it is important to note that a coupling of the $3d\pi_{\Omega'}$ states to the Ar CT states can be ruled out as a source of the observed inverse energetic ordering of the $3d\pi_{\Omega'}$ spin−orbit components. As is illustrated in Figure 10, the largest contributions, although with weights <0.1, that can be attributed to an Ar CT configuration within the $3d\pi_{3/2}$ eigenvector composition, can only be found at Mg−Ar internuclear distances at about 6.6−7.6 a_0. As discussed in the previous section, it is at these internuclear distances where we expect the Ar CT states to cross the Mg-centered $3d\pi_{\Omega'}$ states.

5. CONCLUSIONS AND OUTLOOK

In this article, we have presented a complete set of measurements of the $3d\pi_{1/2}$ and $3d\pi_{3/2}$ Rydberg states of $MgAr^+$, which extends from the lowest vibrational levels ($v' = 0$) up to the dissociation limits. The transitions to low vibrational levels ($v' \lesssim 5$) could be partially rotationally resolved, whereas higher-lying levels were observed as broad diffuse bands. From these measurements, we derived vibrational and rotational constants as well as the dissociation energies. The vibrational level positions and the line widths were interpreted using a model that describes the predissociation interaction of the $3d\pi$ states with the CT states that correlate to the $Mg(3s^2) + Ar^+(^2P_J)$ dissociation limits. As basis states in the model, we used the solutions of the nuclear Schrödinger equation for the individual potential-energy functions using a FEM-DVR method in combination with exterior complex scaling. We also observed high-lying vibrational levels of the $4s\sigma$ state.

The fast predissociation of the $3d\pi$ states is the result of the curve crossings with the CT states, as shown in Figure 9. The CT states have almost twice the bond length of the $3d\pi$ states ($R_e = 4.56\ a_0$ versus $R_e \approx 7.5\ a_0$). Consequently, their repulsive parts intersect the bound regions not only of the $3d\pi$ states, but also of the entire manifold of $MgAr^+$ Rydberg states that belong to series converging on the $MgAr^{2+}\ X^{2+}$ state (see also Figure 1b). The large difference in the bond lengths can be understood in terms of the relevant atomic radii. The bond length of the CT states is determined by the atomic radii of $Mg(3s^2)$ and $Ar^+(^2P_J)$. The $3d\pi$ states, however, are part of a Rydberg series that converges on the $MgAr^{2+}$ ground state and the relevant atomic radii are those from $Mg^{2+}(^1S_0)$ and $Ar(^1S_0)$, as also revealed by the similar bond lengths of the $3d\pi$ ($R_e = 4.56\ a_0$) and X^{2+} ($R_e = 4.38\ a_0$) states. The difference in the atomic radii of ground-state Mg and Mg^{2+} is much larger than for $Ar(^1S_0)$ and $Ar^+(^2P_J)$, which explains the different

bond lengths for the $3d\pi$ and CT states. Comparable bond-length differences are expected for other molecular cations $F_1F_2^+$ forming thermodynamically stable doubly charged cations $F_1F_2^{2+}$ upon ionization; i.e., in general $r_{F_1} \gg r_{F_1^{2+}}$ and $r_{F_2} \approx r_{F_2^+}$, because F_2 is typically much harder than F_1. Consequently, the process of CT-induced predissociation observed in this article is likely to be a general property of the Rydberg states of such cations having the same electronic symmetry as the CT dissociative states.

The electronic coupling elements H_{int} that describe the CT interaction (see Section 4.1) are essentially governed by the following two-electron integral,

$$\langle Mg(3s),\ Mg(3s)|\frac{1}{r_{12}}|Mg^+(3d),\ Ar(3p)\rangle \qquad (14)$$

where r_{12} is the distance between the two electrons. For higher Rydberg states this integral scales as $1/n^{3/2}$, where n is the principal quantum number of the Rydberg electron, according to the well-known scaling of the wave function amplitude at the ionic core.[63,64] The observed line widths of Rydberg states therefore approximately scale with $1/n^3$ (see eq 10). Starting from a line width of 10 cm^{-1} at $n = 3$, representative of our observations for the $3d\pi$ states, we would expect line widths of $\sim 0.0001\ cm^{-1}$ and $\sim 0.004\ cm^{-1}$ (or lifetimes of ~ 50 ns and ~ 1.3 ns) at $n = 130$ and $n = 40$, respectively. These time scales are compatible with measurements we carried out in our recent study on the $MgAr^{2+}$ ground state[28] by PFI-ZEKE photoelectron spectroscopy. In these measurements, the lowest Rydberg states with a $MgAr^{2+}$ core we detected corresponded to $n \approx 130$, which implies that these states have a lifetime of less than 1 μs, compatible with the estimated value obtained from the scaling law (~ 50 ns). The onset of the pulsed-field-ionization signal in PFI-ZEKE photoelectron spectra is thus observed when Stark mixing by stray electric field sets in.[64,65] In the same study,[28] we observed autoionizing resonances corresponding to $MgAr^+$ Rydberg states with principal quantum number $n \sim 40$ and *autoionization* line widths of 0.3 cm^{-1} (corresponding to a lifetime of 180 ps), which is much broader than the predicted CT-induced *predissociation* width at $n = 40$ (see above). This confirms our simple order-of-magnitude estimate of predissociation lifetimes.

The comparably simple structure of $MgAr^+$ and the thermodynamic stability of $MgAr^{2+}$ make the Rydberg states of the $MgAr^+$ ion an ideal model system for studying CT interactions in the Rydberg states of molecular cations. Because the ground state of $MgAr^{2+}$ has a closed-shell electron configuration, the Rydberg states of $MgAr^+$ are effective one-electron systems, if CT-induced predissociation is disregarded. In future work, one may therefore be able to calculate these states using the same approach as the one successfully employed in ref 66 to calculate the Rydberg states of ArH and KrH, extending it to CT processes.

We expect that the results presented here on the structure and dynamics of the Rydberg states of $MgAr^+$ can be transferred to a broader class of singly charged cations. In particular, we expect Rydberg-state dynamics in these systems to be governed by CT-induced predissociation following the general mechanism presented in Figures 1 and 2.

◼ APPENDIX A: PERTURBATIVE CALCULATION OF BOUND-CONTINUUM INTERACTIONS USING EXTERIOR COMPLEX SCALING

We consider the interaction of a bound state $|v\rangle$ with energy E_v with a continuum described by energy-normalized states $|\varepsilon\rangle$. The generalized, complex energy shift F_v is then given by[67]

$$F_v = \lim_{a \to 0^+} \int d\varepsilon \frac{|\langle \varepsilon | H_{\text{int}} | v \rangle|^2}{E_v - \varepsilon + ia} \tag{15}$$

where H_{int} describes the interaction and a is used to regularize the pole at E_v. The choice of sign for a corresponds to outgoing boundary conditions[67] for the bound state $|v\rangle$, which decays because of the interaction with the continuum. The real and imaginary parts of F_v are directly related to the continuum-induced energy shift ΔE_v and width Γ_v of the state $|v\rangle$,

$$F_v \equiv \Delta E_v - i\Gamma_v/2 \tag{16}$$

where ΔE_v and Γ_v are both real. Equation 15 can be rewritten using the Sokhotski-Plemelj theorem,[68] which yields

$$\lim_{a \to 0^+} \int d\varepsilon \frac{|\langle \varepsilon | H_{\text{int}} | v \rangle|^2}{E_v - \varepsilon + ia}$$
$$= \mathcal{P} \int d\varepsilon \frac{|\langle \varepsilon | H_{\text{int}} | v \rangle|^2}{E_v - \varepsilon} - i\pi |\langle \varepsilon | H_{\text{int}} | v \rangle|^2 \Big|_{\varepsilon = E_v} \tag{17}$$

where $\mathcal{P}$ denotes the Cauchy principal value. Comparison of eqs 16 and 17 yields the well-known results for the energy shift and width of state $|v\rangle$,

$$\Delta E_v = \mathcal{P} \int d\varepsilon \frac{|\langle \varepsilon | H_{\text{int}} | v \rangle|^2}{E_v - \varepsilon} \tag{18}$$

$$\Gamma_v = 2\pi |\langle \varepsilon | H_{\text{int}} | v \rangle|^2 \Big|_{\varepsilon = E_v} \tag{19}$$

In the framework of exterior complex scaling (ECS), the numerator in the integrand is given by[69]

$$|\langle \varepsilon | H_{\text{int}} | v \rangle|^2 = \frac{1}{\pi} \text{Im} \sum_i \frac{\langle v_{\theta,i} | H_{\text{int}} | v \rangle^2}{E_{\theta,i} - \varepsilon} \tag{20}$$

where $|v_{\theta,i}\rangle$ and $E_{\theta,i}$ are the complex-rotated eigenvectors and eigenenergies of the continuum channel with rotation angle θ. The energy shift in terms of ECS eigenstates then reads

$$\Delta E_v = \mathcal{P} \int d\varepsilon \frac{1}{E_v - \varepsilon} \frac{1}{\pi} \text{Im} \sum_i \frac{\langle v_{\theta,i} | H_{\text{int}} | v \rangle^2}{E_{\theta,i} - \varepsilon} \tag{21}$$

This integral can be evaluated using the Kramers–Kronig relation for a complex function $f(z)$,

$$\text{Re} f(z) = \frac{1}{\pi} \mathcal{P} \int \frac{\text{Im} f(z')}{z' - z} dz' \tag{22}$$

which gives the result

$$\Delta E_v = -\text{Re} \sum_i \frac{\langle v_{\theta,i} | H_{\text{int}} | v \rangle^2}{E_{\theta,i} - E_v} \tag{23}$$

Comparing eqs 19 and 20 we find for the width

$$\Gamma_v = 2\text{Im} \sum_i \frac{\langle v_{\theta,i} | H_{\text{int}} | v \rangle^2}{E_{\theta,i} - E_v} \tag{24}$$

These results may also be summarized by writing the generalized energy shift in terms of ECS eigenstates as

$$F_v = -\sum_i \frac{\langle v_{\theta,i} | H_{\text{int}} | v \rangle^2}{E_{\theta,i} - E_v} \tag{25}$$

The equations above represent a good approximation to full nonadiabatic calculations (see Section 4.1) if the perturbation introduced by H_{int} is small, i.e., if ΔE_v is small compared to the energy separation to the adjacent bound levels.

◼ AUTHOR INFORMATION

Corresponding Author

Frédéric Merkt − *Laboratory of Physical Chemistry, ETH Zürich, CH-8093 Zürich, Switzerland;*
Email: frederic.merkt@phys.chem.ethz.ch

Authors

Dominik Wehrli − *Laboratory of Physical Chemistry, ETH Zürich, CH-8093 Zürich, Switzerland;* ⊙ orcid.org/0000-0002-6885-8674

Matthieu Génévriez − *Laboratory of Physical Chemistry, ETH Zürich, CH-8093 Zürich, Switzerland*

Stefan Knecht − *Abteilung SHE Chemie, GSI Helmholtzzentrum für Schwerionenforschung, DE-64291 Darmstadt, Germany*

Markus Reiher − *Laboratory of Physical Chemistry, ETH Zürich, CH-8093 Zürich, Switzerland;* ⊙ orcid.org/0000-0002-9508-1565

Complete contact information is available at:
https://pubs.acs.org/10.1021/acs.jpca.1c03859

Notes

The authors declare no competing financial interest.

◼ REFERENCES

(1) Bates, D. R.; Reid, R. H. G. Resonance charge transfer between protons and excited hydrogen atoms I. Quantal two-state approximation. *J. Phys. B: At. Mol. Phys.* **1969**, *2*, 851−856.

(2) Loreau, J.; Ryabchenko, S.; Muñoz Burgos, J. M.; Vaeck, N. Charge transfer in low-energy collisions of H with He$^+$ and H$^+$ with He in excited states. *J. Phys. B: At., Mol. Opt. Phys.* **2018**, *51*, 085205.

(3) Dörfler, A. D.; Eberle, P.; Koner, D.; Tomza, M.; Meuwly, M.; Willitsch, S. Long-range versus short-range effects in cold molecular ion-neutral collisions. *Nat. Commun.* **2019**, *10*, 5429.

(4) MacAdam, K. B.; Day, J. C.; Aguilar, J. C.; Homan, D. M.; MacKellar, A. D.; Cavagnero, N. J. Transient molecular-ion formation in Rydberg-electron capture. *Phys. Rev. Lett.* **1995**, *75*, 1723−1726.

(5) Capitelli, M.; Lamanna, U. Collision integrals of electronically excited states and transport coefficients of thermal plasmas. *J. Plasma Phys.* **1974**, *12*, 71−79.

(6) Kosarim, A. V.; Smirnov, B. M.; Laricchiuta, A.; Capitelli, M. Resonant charge-exchange involving excited helium atoms and reactive transport of local thermodynamic equilibrium helium plasma. *Phys. Plasmas* **2012**, *19*, 062309.

(7) Dalgarno, A.; Yadav, H. N. Electron capture II: Resonance capture from hydrogen atoms by slow protons. *Proc. Phys. Soc., London, Sect. A* **1953**, *66*, 173−177.

(8) Janev, R. K.; Joachain, C. J.; Nedeljković, N. N. Resonant electron transfer in slow collisions of protons with Rydberg hydrogen atoms. *Phys. Rev. A: At., Mol., Opt. Phys.* **1984**, *29*, 2463−2469.

(9) Muñoz Burgos, J. M.; Griener, M.; Loreau, J.; Gorbunov, A.; Lunt, T.; Schmitz, O.; Wolfrum, E. Evaluation of emission contributions from charge-exchange between the excited states of deuterium with He^+ during diagnostic of thermal helium gas beam injection and laser-induced fluorescence. *Phys. Plasmas* **2019**, *26*, 063301.

(10) Hinojosa, G.; Covington, A. M.; Phaneuf, R. A.; Sant'Anna, M. M.; Hernandez, R.; Covington, I. R.; Domínguez, I.; Bozek, J. D.; Schlachter, A. S.; Alvarez, I.; et al. Formation of long-lived CO^{2+} via photoionization of CO^+. *Phys. Rev. A: At., Mol., Opt. Phys.* **2002**, *66*, 032718.

(11) Douix, S.; Duflot, D.; Cubaynes, D.; Bizau, J.-M.; Giuliani, A. Photoionization of the Buckminsterfullerene cation. *J. Phys. Chem. Lett.* **2017**, *8*, 7−12.

(12) Wenzel, G.; Joblin, C.; Giuliani, A.; Rodriguez Castillo, S.; Mulas, G.; Ji, M.; Sabbah, H.; Quiroga, S.; Peña, D.; Nahon, L. Astrochemical relevance of VUV ionization of large PAH cations. *Astron. Astrophys.* **2020**, *641*, A98.

(13) Lefebvre-Brion, H.; Field, R. W. *The Spectra and Dynamics of Diatomic Molecules*; Elsevier: Amsterdam, 2004.

(14) Herzberg, G. *Molecular Spectra and Molecular Structure, Vol. I, Spectra of Diatomic Molecules*, 2nd ed.; Van Nostrand Reinhold Company: New York, 1950.

(15) Mulliken, R. S. The Rydberg states of molecules. Parts I-V. *J. Am. Chem. Soc.* **1964**, *86*, 3183−3197.

(16) Mulliken, R. S. The Rydberg states of molecules. VI. Potential curves and dissociation behavior of (Rydberg and other) diatomic states. *J. Am. Chem. Soc.* **1966**, *88*, 1849−1861.

(17) Mulliken, R. S. Rydberg states of molecules. VII. *J. Am. Chem. Soc.* **1969**, *91*, 4615−4621.

(18) Bates, D. R.; Reid, R. H. G. Electronic eigenenergies of the hydrogen molecular ion. *Adv. At. Mol. Phys.* **1968**, *4*, 13−35.

(19) Teller, E. Über das Wasserstoffmolekülion. *Z. Phys.* **1930**, *61*, 458−480.

(20) Ordóñez-Lasso, A. F.; Martín, F.; Sanz-Vicario, J. L. Screening effects on the electronic structure of the hydrogen molecular ion. *Phys. Rev. A: At., Mol., Opt. Phys.* **2017**, *95*, 012504.

(21) Jungen, M.; Jungen, Ch. Rydberg states of the HeH^+ ion calculated by *ab initio* methods: potential energies and effective principal quantum numbers. *Mol. Phys.* **2015**, *113*, 2333−2343.

(22) Bouhali, I.; Bezzaouia, S.; Telmini, M.; Jungen, Ch. Rydberg and continuum states of the HeH^+ molecular ion: Variational R-matrix and multichannel quantum defect theory calculations. *Phys. Rev. A: At., Mol., Opt. Phys.* **2016**, *94*, 022516.

(23) Green, T. A.; Michels, H. H.; Browne, J. C.; Madsen, M. M. Configuration interaction studies of the HeH^+ molecular ion. I Singlet sigma states. *J. Chem. Phys.* **1974**, *61*, 5186−5197.

(24) Pauling, L. The normal state of the helium molecule-ions He_2^+ and He_2^{+2}. *J. Chem. Phys.* **1933**, *1*, 56−59.

(25) Dunitz, J. D.; Ha, T. K. Non-empirical SCF calculations on hydrogen-like molecules: the effect of nuclear charge on binding energy and bond length. *J. Chem. Soc., Chem. Commun.* **1972**, 568−569.

(26) Guilhaus, M.; Brenton, A. G.; Beynon, J. H.; Rabrenović, M.; von Ragué Schleyer, P. First observation of He_2^{2+}: charge stripping of He_2^+ using a double-focusing mass spectrometer. *J. Phys. B: At. Mol. Phys.* **1984**, *17*, L605−L610.

(27) Maier, J. P. Spectroscopic characterization of cations: from photoelectron spectroscopy to laser and ion-beam methods. *J. Electron Spectrosc. Relat. Phenom.* **1993**, *66*, 15−24.

(28) Wehrli, D.; Génévriez, M.; Merkt, F. Spectroscopic characterization of a thermodynamically stable doubly charged molecule: $MgAr^{2+}$. *Phys. Chem. Chem. Phys.* **2021**, *23*, 10978−10987.

(29) Gardner, A. M.; Withers, C. D.; Graneek, J. B.; Wright, T. G.; Viehland, L. A.; Breckenridge, W. H. Theoretical Study of M^+−RG and M^{2+}−RG Complexes and Transport of M^+ through RG (M = Be and Mg, RG = He−Rn). *J. Phys. Chem. A* **2010**, *114*, 7631−7641.

(30) Pilgrim, J. S.; Yeh, C. S.; Duncan, M. A. Photodissociation spectroscopy of Mg^+−Ar. *Chem. Phys. Lett.* **1993**, *210*, 322−326.

(31) Pilgrim, J. S.; Yeh, C. S.; Berry, K. R.; Duncan, M. A. Photodissociation spectroscopy of Mg^+-rare gas complexes. *J. Chem. Phys.* **1994**, *100*, 7945−7956.

(32) Yeh, C. S.; Pilgrim, J. S.; Willey, K. F.; Robbins, D. L.; Duncan, M. A. Spectroscopy of weakly-bound magnesium ion complexes. *Int. Rev. Phys. Chem.* **1994**, *13*, 231−262.

(33) Scurlock, C. T.; Pilgrim, J. S.; Duncan, M. A. Rotationally resolved photodissociation spectroscopy of Mg^+-Ar. *J. Chem. Phys.* **1995**, *103*, 3293−3298. Scurlock, C. T.; Pilgrim, J. S.; Duncan, M. A. Erratum: Rotationally resolved photodissociation spectroscopy of Mg$^+$ −Ar [J. Chem. Phys. 103, 3293 (1995)]. *J. Chem. Phys.* **1996**, *105*, 7876.

(34) Génévriez, M.; Wehrli, D.; Merkt, F. High-resolution spectroscopy of the $A^+\ ^2\Pi_{\Omega'=1/2,3/2} \leftarrow X^+\ ^2\Sigma^+$ transition of $MgAr^+$ by isolated-core multiphoton Rydberg dissociation. *Mol. Phys.* **2020**, *118*, No. e1703051.

(35) Wehrli, D.; Génévriez, M.; Knecht, S.; Reiher, M.; Merkt, F. Complete characterization of the 3p Rydberg complex of a molecular ion: $MgAr^+$. I. Observation of the $Mg(3p_\sigma)Ar^+\ B^+$ state and determination of its structure and dynamics. *J. Chem. Phys.* **2020**, *153*, 074310.

(36) Génévriez, M.; Wehrli, D.; Merkt, F. Complete characterization of the 3p Rydberg complex of a molecular ion: $MgAr^+$. II. Global analysis of the $A^+\ ^2\Pi$ and $B^+\ ^2\Sigma^+$ ($3p_{\sigma,\pi}$) states. *J. Chem. Phys.* **2020**, *153*, 074311.

(37) Génévriez, M.; Wehrli, D.; Agner, J. A.; Merkt, F. PFI-ZEKE photoelectron spectroscopy of positively charged ions: illustration with Mg^+. *Int. J. Mass Spectrom.* **2019**, *435*, 209−216.

(38) Wehrli, D.; Génévriez, M.; Kreis, C.; Agner, J. A.; Merkt, F. Determination of the interaction potential and rovibrational structure of the ground electronic State of $MgAr^+$ using PFI-ZEKE photoelectron spectroscopy. *J. Phys. Chem. A* **2020**, *124*, 379−385.

(39) Zare, R. N. *Angular Momentum*; John Wiley & Sons: New York, 1988.

(40) Brown, J. M.; Carrington, A. *Rotational Spectroscopy of Diatomic Molecules*; Cambridge University Press: Cambridge, U.K., 2003.

(41) Kramida, A.; Ralchenko, Y.; Reader, J.; *NIST ASD Team, NIST Atomic Spectra Database* (ver. 5.6.1), [Online]. Available: https://physics.nist.gov/asd [2020, May 25]. National Institute of Standards and Technology: Gaithersburg, MD., 2019.

(42) Cohen, J. S.; Schneider, B. Ground and excited states of Ne_2 and Ne_2^+. I. Potential curves with and without spin-orbit coupling. *J. Chem. Phys.* **1974**, *61*, 3230−3239.

(43) Wüest, A.; Merkt, F. Potential energy curves of diatomic molecular ions from high-resolution photoelectron spectroscopy. I. The first six electronic states of Ar_2^+. *J. Chem. Phys.* **2004**, *120*, 638−646.

(44) Born, M.; Mayer, J. E. Zur Gittertheorie der Ionenkristalle. *Z. Phys.* **1932**, *75*, 1−18.

(45) Schwerdtfeger, P.; Nagle, J. K. 2018 Table of static dipole polarizabilities of the neutral elements in the periodic table. *Mol. Phys.* **2019**, *117*, 1200−1225.

(46) Tang, K. T.; Toennies, J. P. An improved simple model for the van der Waals potential based on universal damping functions for the dispersion coefficients. *J. Chem. Phys.* **1984**, *80*, 3726−3741.

(47) Manolopoulos, D.; Wyatt, R. Quantum scattering via the log derivative version of the Kohn variational principle. *Chem. Phys. Lett.* **1988**, *152*, 23−32.

(48) Rescigno, T. N.; McCurdy, C. W. Numerical grid methods for quantum-mechanical scattering problems. *Phys. Rev. A: At., Mol., Opt. Phys.* **2000**, *62*, 032706.

(49) Simon, B. The definition of molecular resonance curves by the method of exterior complex scaling. *Phys. Lett. A* **1979**, *71*, 211−214.

(50) Lessinger, L. Morse oscillators, Birge-Sponer extrapolation, and the electronic absorption spectrum of I_2. *J. Chem. Educ.* **1994**, *71*, 388−391.

(51) Fano, U. Effects of configuration interaction on intensities and phase shifts. *Phys. Rev.* **1961**, *124*, 1866−1878.

(52) Fleig, T.; Olsen, J.; Visscher, L. The generalized active space concept for the relativistic treatment of electron correlation. II. Large-scale configuration interaction implementation based on relativistic 2- and 4-spinors and its application. *J. Chem. Phys.* **2003**, *119*, 2963−2971.

(53) Knecht, S.; Jensen, H. J. Aa.; Fleig, T. Large-scale parallel configuration interaction. II. Two and four-component double-group general active space implementation with application to BiH. *J. Chem. Phys.* **2010**, *132*, 014108.

(54) Jensen, H. J. Aa. *Douglas−Kroll the Easy Way*; Talk at Conference on Relativistic Effects in Heavy Elements - REHE, Mülheim, Germany, April, 2005. Available at DOI: 10.6084/m9.figshare.12046158.

(55) Kutzelnigg, W.; Liu, W. Quasirelativistic theory equivalent to fully relativistic theory. *J. Chem. Phys.* **2005**, *123*, 241102.

(56) Iliaš, M.; Saue, T. An infinite-order two-component relativistic Hamiltonian by a simple one-step transformation. *J. Chem. Phys.* **2007**, *126*, 064102.

(57) Hess, B. A.; Marian, C. M.; Wahlgren, U.; Gropen, O. A mean-field spin-orbit method applicable to correlated wavefunctions. *Chem. Phys. Lett.* **1996**, *251*, 365−371.

(58) Sikkema, J.; Visscher, L.; Saue, T.; Iliaš, M. The molecular mean-field approach for correlated relativistic calculations. *J. Chem. Phys.* **2009**, *131*, 124116.

(59) Dunning, T. H., Jr. Gaussian basis sets for use in correlated molecular calculations. I. The atoms boron through neon and hydrogen. *J. Chem. Phys.* **1989**, *90*, 1007−1023.

(60) Thyssen, J. *Development and Applications of Methods for Correlated Relativistic Calculations of Molecular Properties*. Dissertation, Department of Chemistry, University of Southern Denmark: 2001.

(61) Gomes, A. S. P.; Saue, T.; Visscher, L.; Jensen, H. J. Aa.; Bast, R., with contributions from Aucar, I. A.; Bakken, V.; Dyall, K. G.; Dubillard, S.; Ekström, U.; et al. *DIRAC, a relativistic ab initio electronic structure program, Release DIRAC19* (2019) (available at DOI: 10.5281/zenodo.3572669; see also http://www.diracprogram.org).

(62) Saue, T.; Bast, R.; Gomes, A. S. P.; Jensen, H. J. Aa.; Visscher, L.; Aucar, I. A.; di Remigio, R.; Dyall, K. G.; Eliav, E.; Faßhauer, E.; et al. The DIRAC code for relativistic molecular calculations. *J. Chem. Phys.* **2020**, *152*, 204104.

(63) Gallagher, T. F. *Rydberg Atoms*; Cambridge University Press: Cambridge, U.K., 1994.

(64) Merkt, F. Molecules in high Rydberg states. *Annu. Rev. Phys. Chem.* **1997**, *48*, 675−709.

(65) Chupka, W. A. Factors affecting lifetimes and resolution of Rydberg states observed in zero-electron-kinetic-energy spectroscopy. *J. Chem. Phys.* **1993**, *98*, 4520−4530.

(66) Jungen, Ch.; Roche, A. L.; Arif, M. The Rydberg spectrum of ArH and KrH: calculation by *R*-matrix and generalized quantum defect theory. *Philos. Trans. R. Soc., A* **1997**, *355*, 1481−1506.

(67) Faisal, F. H. M. *Theory of multiphoton processes*; Springer: 1987.

(68) Vladimirov, V. S. In *Equations of Mathematical Physics*; Jeffrey, A., Ed.; Marcel Dekker, Inc.: 1971.

(69) Rescigno, T. N.; McKoy, V. Rigorous method for computing photoabsorption cross sections from a basis-set expansion. *Phys. Rev. A: At., Mol., Opt. Phys.* **1975**, *12*, 522−525.